

Importance of Considering Near-Surface Attenuation in Earthquake Source Parameter Estimation: Insights from Kappa at a Dense Array in Oklahoma

Hilary Chang^{*1}, Rachel E. Abercrombie², and Nori Nakata^{1,3}

ABSTRACT

Separating earthquake source spectra from propagation effects is challenging. The propagation effect contains a site-dependent term related to the high attenuation of shallow sediments. Neglecting the site-dependent attenuation can cause large biases and scattering in the corner-frequency (f_c) estimates, resulting in significant stress-drop deviations. In this study, we investigate shallow attenuation at the LArge-*n* Seismic Survey in Oklahoma (LASSO) and site-related biases and scattering in source parameter measurements due to simplified attenuation models. We measure the high-frequency spectral decay parameter kappa on the vertical acceleration spectra of regional earthquakes (125 km away). The site-dependent kappa ($\kappa_{0,acc}$) suggests that attenuation increases rapidly at shallow depth and is highly site-dependent. 10%–75% of the attenuation is site-dependent for S waves and even larger for P waves. The quality factor for S waves (Q_S) ranges from 10 to 100 in the upper 400 m. Q_P for P waves is mostly below 10 within the same depth. The Quaternary sediments tend to be more attenuating ($Q_S < 30$), but the Permian rocks also can have high attenuation. We demonstrate that using a non-site-dependent attenuation model in single-spectra fitting leads to large scattering in f_c estimates among stations with apparent good fits. The apparent f_c can significantly deviate when the range of site-dependent kappa is large or with a higher assumed source spectral fall-off rate n . The biases in apparent f_c depend on site condition and distance; however, the correlation between f_c and these factors might not be obvious, depending on model assumptions. An apparent increase of stress drop with magnitude in a previous study for local microearthquakes ($1.3 < M_w < 3.0$) can be largely negated by including a site term, restricting to sites on the higher Q formations, and fixing n . This study highlights the importance of considering near-surface attenuation when modeling source parameters.

KEY POINTS

- Attenuation is dominantly site-dependent in the central United States.
- Neglecting shallow attenuation causes large uncertainties and biases despite apparently small model misfits.
- Having controlled site conditions is more important than using many stations in estimating source parameters.

Supplemental Material

in which f is frequency, $u(f)$ is the recorded particle displacement, velocity, or acceleration spectrum, $s(f)$ is the source model, $p(f)$ is the path term that describes the path-dependent attenuation, and $g(f)$ is the site-dependent term. The site term is associated with, for example, shallow unconsolidated

1. Department of Earth, Atmospheric, and Planetary Sciences, Massachusetts Institute of Technology, Cambridge, Massachusetts, U.S.A.,  <https://orcid.org/0000-0002-9402-6089> (HC);  <https://orcid.org/0000-0002-9295-9416> (NN); 2. Department of Earth and Environment, Boston University, Boston, Massachusetts, U.S.A.,  <https://orcid.org/0000-0003-4515-5420> (REA); 3. Lawrence Berkeley National Laboratory, Berkeley, California, U.S.A.

*Corresponding author: hilarych@mit.edu

Cite this article as Chang, H., R. E. Abercrombie, and N. Nakata (2025). Importance of Considering Near-Surface Attenuation in Earthquake Source Parameter Estimation: Insights from Kappa at a Dense Array in Oklahoma, *Bull. Seismol. Soc. Am.*, XX, 1–18, doi: [10.1785/0120240137](https://doi.org/10.1785/0120240137)

© Seismological Society of America

sediments that have higher attenuation and resonance effects. Incorrect separation of the path and site terms can bias measurements of source parameters such as stress drop (Abercrombie, 1995).

Earthquake stress drop characterizes the energy released and is an important parameter for understanding source physics, rupture simulation, and ground-motion modeling. However, the stress drop not only depends on how it is defined (Atkinson and Beresnev, 1997; Ji *et al.*, 2022) but the measurements are also highly variable (Allmann and Shearer, 2009; Abercrombie *et al.*, 2016; Cocco *et al.*, 2016; Oth *et al.*, 2017). The stress-drop estimates can deviate for moderate-to-small events due to the resolution limit, which then causes apparent breakdowns in earthquake self-similarity (Abercrombie, 1995, 2021). The recent Community Stress-Drop Validation Project (Abercrombie *et al.*, 2024; Baltay *et al.*, 2024) has revealed highly variable measurements for the 2019 Ridgecrest earthquake sequence among different research teams. They found that the stress-drop estimates vary due to methods and assumptions (Abercrombie *et al.*, 2024; Shearer *et al.*, 2024). Although many of the research teams observed an increase in stress drops with earthquake magnitude, which implies a larger rupture dimension generates events with higher magnitudes, the observations are still within the range of uncertainty of a constant stress drop. Whether the observed earthquake scaling is due to method biases, simplified assumptions, or actual indications of non-self-similarity is still under debate.

One of the biggest uncertainties in stress-drop estimates comes from the corner frequency (f_c) (Abercrombie, 2021). Earthquake stress drops for a circular crack can be modeled as (Eshelby, 1957; Brune, 1970; Madariaga, 1976)

$$\Delta\sigma = \frac{7}{16} \left(\frac{f_c}{k\beta} \right)^3 M_0, \quad (2)$$

in which f_c relates to the source dimension, M_0 is the seismic moment, k is a constant depending on the wave type and the rupture model, and β is the shear-wave velocity at the source focal depth. f_c is highly sensitive to the shape of the earthquake spectra and exhibits a notorious trade-off with attenuation (Anderson, 1986; Boore, 1986; Ko *et al.*, 2012). The uncertainty in f_c is magnified by the power of three (equation 2), causing significant biases in the calculated stress drop, which increases with earthquake magnitudes (Abercrombie, 1995). Edwards and Rietbrock (2009) found strong trade-offs between attenuation and f_c that they could not determine whether stress drops are constant or increasing with magnitudes with their high-quality High Sensitivity Seismograph Network and Kiban-Kyoshin network datasets in Japan.

There are several approaches to address propagation effects in source spectra modeling. The single-spectra method models the earthquake spectra directly with assumed attenuation structures (e.g., Ko *et al.*, 2012; Supino *et al.*, 2019). The

single-spectra method can be difficult because of irregularities in the spectra and limited bandwidth (Shearer, 2009) and is subject to parameter trade-offs (Ko *et al.*, 2012). Another method is the spectral ratio—the empirical Green's functions (EGFs) approach. The spectral ratio method uses co-located small events with the same focal mechanism as the EGFs to remove propagation effects (Hartzell, 1978; Hough, 1997; Mayeda *et al.*, 2007; Abercrombie, 2015), and is quite effective (e.g., Chang *et al.*, 2023). The advantage of using EGF is that we do not need to assume an attenuation model. However, a qualified small event is often not available (especially for microearthquakes), and the selection and modeling of the small event brings in other uncertainties (Abercrombie, 2015; Shearer *et al.*, 2019). Large-scale inversion methods, including the generalized inversion technique (GIT; Andrews, 1986; Castro *et al.*, 1990; Hartzell, 1992; Oth *et al.*, 2011; Bindi *et al.*, 2020), and spectral decomposition (e.g., Shearer *et al.*, 2006, 2019), derive nonparametric site response spectra to correct the relative source spectra obtained from an inversion. However, for the source, path, and site terms to be properly constrained in the inversion, a dataset with these terms well-traversed in the parameter space is required. In addition, the inversion still suffers from parameter trade-offs (Shearer *et al.*, 2019; Bindi *et al.*, 2023, 2024), including between f_c , M_0 , $\Delta\sigma$, the high-frequency fall-off rate, and attenuation.

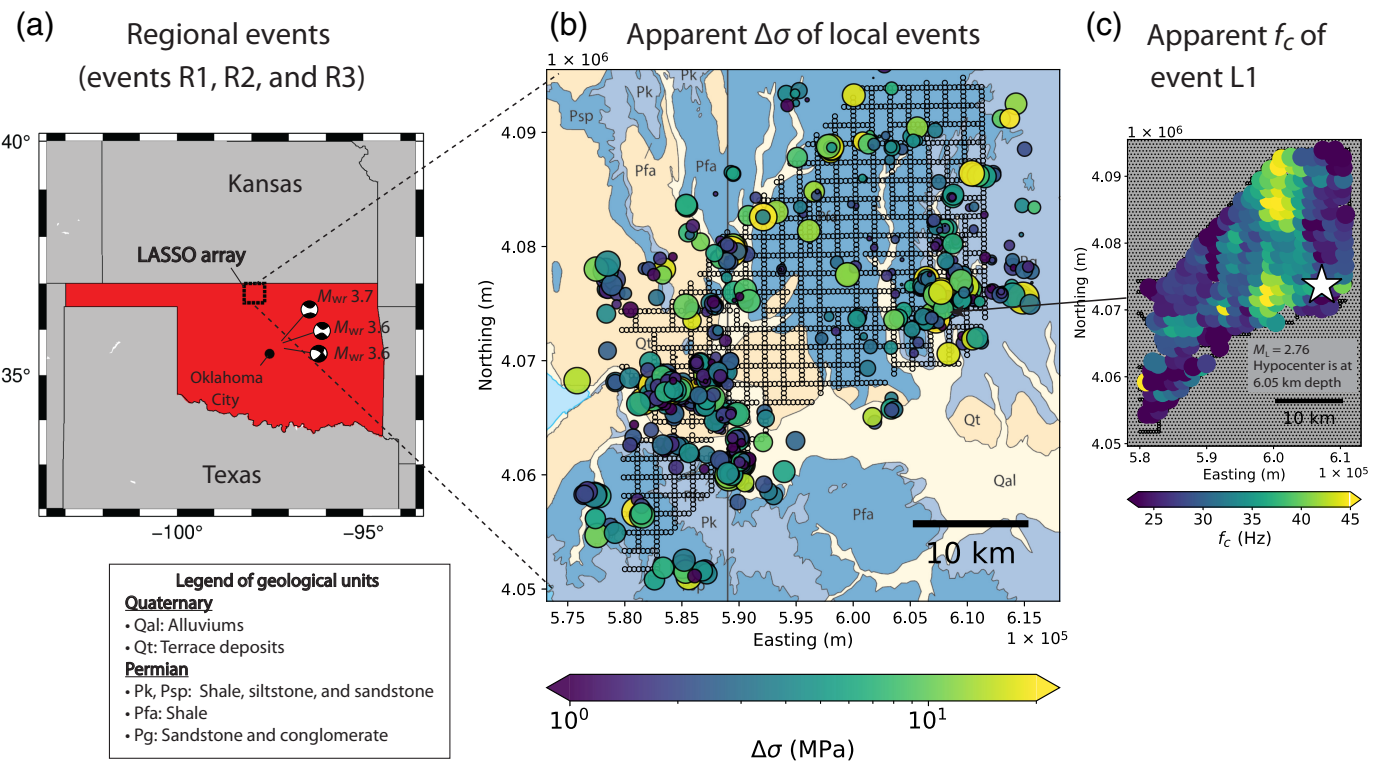
Both the single-spectra method and the spectral decomposition require some assumptions on the attenuation model. In this study, we focus on the single-spectra approach to investigate the trade-off between f_c and attenuation in source spectral modeling when using an oversimplified attenuation model. We note that this trade-off can occur not only in the single-spectra approach but also in any approach that requires assuming the attenuation model for modeling the earthquake spectra.

The single-spectra approach models the far-field earthquake displacement spectrum and the attenuation as (Ω_t) (Brune, 1970; Boatwright, 1978, 1980),

$$\Omega_t(f) = \frac{\Omega_0}{[1 + (f/f_c)^n]^{1/\gamma}} \cdot e^{-\pi f \kappa}, \quad (3)$$

in which Ω_0 is the long-period spectral amplitude, n is the high-frequency fall-off rate, and γ is 1 or 2 depending on whether using a Brune or Boatwright model. The exponential term characterizes the frequency-dependent path effect (Anderson and Hough, 1984). The attenuation parameter kappa (κ) is the integration of travel time (tt_i) divided by a quality factor (Q_i , assumed to be frequency independent) across each layer i along the propagation path (Hough and Anderson, 1988):

$$\kappa = \int_{\text{path}} \frac{tt_i}{Q_i}. \quad (4)$$



A tempting (but often wrong) assumption is that κ is nearly proportional to travel time. For example, the single-spectra fitting approaches in Supino *et al.* (2019) and Kemna *et al.* (2020, 2021) assumed that attenuation is travel time divided by a constant Q without a site-dependent attenuation term. This simplification raises concerns because attenuation along the path is often far from evenly distributed.

Although the average crustal Q is in the range of hundreds to thousands (Singh and Herrmann, 1983; Benz *et al.*, 1997; Levandowski *et al.*, 2021), the near-surface layers generally have a much lower Q . Borehole data in California (Jongmans and Malin, 1995; Abercrombie, 1998) and Switzerland (Bethmann *et al.*, 2012) showed Q less than 30 in the top 0.5 km. Abercrombie (1997) found that 90% of the attenuation for earthquakes with an epicentral distance under 15 km occurs in the upper 3 km in the Cajon Pass borehole in California, whereas half of the attenuation occurs in the upper 300 m. We will show that neglecting the site-dependent term in κ can result in large scattering and bias.

The LArge- n Seismic Survey in Oklahoma (LASSO; Fig. 1; Dougherty *et al.*, 2019), with 1825 vertical-component nodal geophones, provides an unprecedented dataset with which to examine the site conditions and source parameter variabilities. The dense station coverage with large (moment magnitudes $M_{wr} > 3$) distant events that are relatively equidistant from the stations allows a thorough investigation of the apparent attenuation on a flat basin plain. We measure the kappa on the acceleration spectra (denoted as κ_{acc}) of the large distant earthquakes. The site-dependent part of kappa ($\kappa_{0,acc}$) relates to site properties such as the average shear-wave velocity in the

Figure 1. Regional and local earthquakes recorded at the LArge- n Seismic Survey in Oklahoma (LASSO) array and the variability of source parameter measurements using a single-spectra fitting approach. (a) The focal mechanisms and the moment magnitudes (M_{wr}) are for the three largest regional earthquakes (events R1, R2, and R3) 126–178 km from the array. The small dashed box marks the array location. (b) The colored circles are local events. The colors indicate apparent stress drop ($\Delta\sigma$) based on the single-spectra measurements in (Kemna *et al.*, 2020) (denoted as KN20). The size of the circles is proportional to local magnitudes ($M_L = 0.01$ –3.0). The small, black, hollow circles are stations. The map shows the surface geology (see the legend on the lower left; Heran *et al.*, 2003). (c) We show the corner frequency (f_c) estimates using the single-spectra approach for a local event (event L1; the white star marks the epicenter) in KN20. Each colored dot in panel (c) represents the median f_c measured by a subarray that includes stations within a 2.5 km diameter circle. The color version of this figure is available only in the electronic edition.

top 30 m (V_{S30} ; e.g., Van Houtte *et al.*, 2011) and is an important parameter in ground-motion modeling (PEER, 2015).

We use $\kappa_{0,acc}$ to estimate the apparent site attenuation that might apply to the spectra of local earthquakes. Our approach avoids narrowband amplifications. However, we do not attempt to fully quantify the potential broadband amplification (e.g., Boore and Joyner, 1997; Campbell and Bozorgnia, 2014) and attenuation in the kappa values. We compare the kappa values with the source parameters of local microearthquakes (local magnitudes or $M_L < 3$) estimated using the single-spectra method from a previous study (Kemna *et al.*, 2020). We show that the source parameter variabilities can be reproduced using our independent kappa measurements from distant events.

LASSO ARRAY AND THE DATA

The LASSO array is located on a flat plain in the northern Anadarko basin, with less than 100 m relief in total (Crain and Chang, 2018). The top 2 km consists of sedimentary rocks from the Permian to Cambrian ages (Johnson and Luza, 2008). The Quaternary alluvium and terrace deposits cover locally with a thickness of a few to tens of meters (Fig. 1b; Heran *et al.*, 2003). The array contains 1825 stations in an area of 25 km × 32 km with the minimum station spacing of 400 m. The stations are velocity sensors, the Fairfield Nodal vertical-component 10 Hz nodes, with a sampling rate of 500 Hz. The array was deployed from mid-April to mid-May in 2016 for about a month, during which it recorded more than a thousand microearthquakes associated with wastewater injections with local magnitudes ranging from 0.01 to 3.0 (Cochran *et al.*, 2020). The majority of these events occurred between 1.5 and 5.5 km in depth. The array also recorded a few distant events from central Oklahoma with moment magnitudes (M_{wr}) >3.6 (Fig. 1a; 126–178 km away; U.S. Geological Survey [USGS], 2022).

Kemna *et al.* (2020) (denoted as KN20 thereafter) used both a single-spectra fitting approach (equation 3) and a spectral ratio approach to calculate source parameters, including corner frequency (f_c), seismic moment (M_0), and stress drop ($\Delta\sigma$). Although their spectral ratio method results do not show an increase of stress drop with magnitudes, the single-spectra method results do, with the biases in f_c and $\Delta\sigma$ correlated with surficial geology (Fig. 1b,c; Chang *et al.*, 2023). Both methods exhibit large scattering among stations. Chang *et al.* (2023) attempted to correct the apparent bias in the single-spectra results using surface ground motions as a proxy; however, large scattering with unknown causes remains after the correction. In their single-spectra approach, KN20 assumed $\kappa = tt/Q$. They performed a grid search to find a combination of $Q = 600$ and $n = 3.5$ that yielded the overall best fit. They used either the Brune ($\gamma = 1$) or the Boatwright model ($\gamma = 2$), depending on which fits better. Later, we will find out the cause of the large scattering with synthetic tests using these fitting criteria.

The large number of stations (nearly 2000) means that we can group them into subarrays to improve stability and resolution and still retain significant spatial variation. We group the stations into 272 subarrays. Each subarray consists of stations within a circle of 2.5 km diameter (15–20 stations). In the following analysis, we stack spectra in each subarray and take the median measurements from KN20 among the stations in a subarray. The spectra and data points in the figures represent averaged values in subarrays instead of individual stations. By averaging among stations, we reduce the impact of local resonances and outliers.

SHALLOW ATTENUATION ACROSS THE LASSO ARRAY

We estimate the high-frequency spectral decay parameter κ_{acc} on the Fourier acceleration spectra based on Anderson and Hough (1984),

$$\kappa_{acc} = -\frac{1}{\pi} \frac{d(\ln(A))}{df}, \quad (5)$$

in which $\frac{d(\ln(A))}{df}$ is the slope of the acceleration spectrum in linear-log space and has a unit of seconds. The measured κ_{acc} has a site-dependent component $\kappa_{0,acc}$ and a distance-dependent component $\kappa_{r,acc}$. The site component $\kappa_{0,acc}$ can be derived by removing a linear dependence between κ_{acc} and epicentral distances (Ktenidou *et al.*, 2015).

We use three regional earthquakes in central Oklahoma (moment magnitudes M_{wr} 3.6–3.7; R1–R3 in Table S1, available in the supplemental material to this article) to estimate $\kappa_{p,acc}$ for P arrivals and $\kappa_{s,acc}$ for S arrivals. To calculate the Fourier acceleration spectra, we first demean, detrend, taper, and prefilter the raw data. Then, we remove the instrument response and convert the data to acceleration using ObsPy with the response file provided by the manufacturer. We put a water level of 40 to avoid amplifying noise below 1 Hz when removing the responses. After the data conversion, we cut the 1.5 s window starting at 0.15 s before the arrivals. A short time window can avoid scattering effects that would result in an underestimated attenuation (Parolai *et al.*, 2022). The arrivals are estimated using a similar approach in Chang *et al.* (2023): we first estimate the arrivals by raytracing with the velocity model from Rubinstein *et al.* (2018). Then, we visually examine the predicted moveout and adjust small time shifts of the arrival for each event. The amplitude spectra are calculated using the multitaper method (Prieto, 2022). See Text S1 for more details on data processing.

It is important to measure kappa beyond the site-amplification resonance peaks and the corner frequency of the earthquake source. We follow a similar approach as Nye *et al.* (2023) to select the start of the frequency band (Fig. 2). First, we fit the acceleration spectra with a degree-15 polynomial. Then, we calculate the first derivative of the polynomial. The minimum of the first derivatives is where the largest amplitude drop occurs. The start of the frequency band is the minimum of the first derivative (Nye *et al.*, 2023) or 1.5 times the corner frequency (Ktenidou *et al.*, 2016), depending on which one is higher. Events R1–R3 have corner frequencies between 2 and 5 Hz based on spectra observed on the rock sites. The end of the frequency band is where the signal-to-noise ratio (SNR) drops below 3 (Ktenidou *et al.*, 2016). The SNR is defined as the ratio between the spectral amplitude of the signal to that of the noise, which is calculated in a 1.5 s window, 8 s before the P arrivals. The majority of $\kappa_{p,acc}$ are measured between 10 and 30 Hz; and for $\kappa_{s,acc}$, the majority are between 12 and 45 Hz (Fig. S1).

To avoid narrowband resonances, we require the minimum frequency bandwidth of 15 Hz, where the spectra show linearly decaying trends on the semilog scale (Fig. 3). For P waves, sites with higher kappa have lower amplitudes above 20 Hz

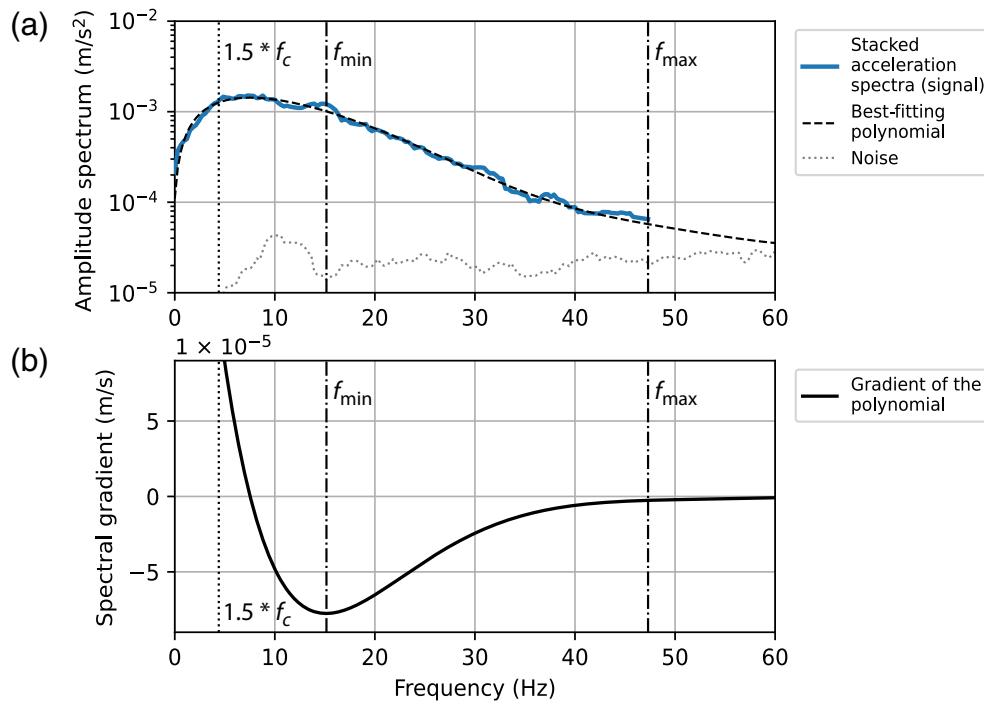


Figure 2. The frequency band selection criteria for measuring kappa (κ_{acc}). (a) The solid and dotted spectra are the acceleration spectra for the S arrival and noise, respectively. The spectra are stacked among stations in the subarray (15–20 stations). We fit the spectra with a degree-15 polynomial (dashed curve in panel a) and calculate the first derivative of the polynomial (solid curve in panel b). We measure $\kappa_{\text{s,acc}}$ on the spectra between f_{min} and f_{max} (vertical dashed dotted lines). f_{min} is at the bottom of the valley of the first derivative. f_{max} is just before where the signal-to-noise ratio (SNR) starts to drop below three. We require $f_{\text{min}} > 1.5 \times$ the corner frequency (f_c) (vertical dotted line). f_c is between 2 and 5 Hz for the three regional events.

compared with other sites. For S waves, sites with higher kappa have higher amplitudes below 25 Hz and lower amplitudes above 30 Hz compared with other sites. The κ_{acc} captures

the apparent spectral attenuation that spans a wide frequency range.

Figure 4 shows $\kappa_{p,\text{acc}}$ and $\kappa_{s,\text{acc}}$ measured from the large distant events. The kappa values are strongly site dependent. $\kappa_{p,\text{acc}}$ is mostly limited to Permian formations (Fig. 4a) because of limited bandwidth on the Quaternary sites for P waves. $\kappa_{s,\text{acc}}$ shows higher values (>0.03 s) on the Quaternary formations and on the southwest side of the array (Fig. 4b). In Figure 4c, $\kappa_{p,\text{acc}}/\kappa_{s,\text{acc}} > 1$ in general, which suggests P waves exhibit higher spectral decay than S waves. If we relax the minimum bandwidth to 10 Hz to include more measurements on the Quaternary sites (Fig. S2), the higher $\kappa_{p,\text{acc}}$ and $\kappa_{s,\text{acc}}$ are both on the Quaternary sites and $\kappa_{p,\text{acc}}$ and $\kappa_{s,\text{acc}}$ have a weak correlation (cross-correlation coefficient = 0.3).

However, relaxing the mini-

mum bandwidth to 10 Hz is likely subject to amplitude bulges between 10 and 20 Hz (Fig. S3). Hence, we choose to stick to the 15 Hz minimum bandwidth requirement.

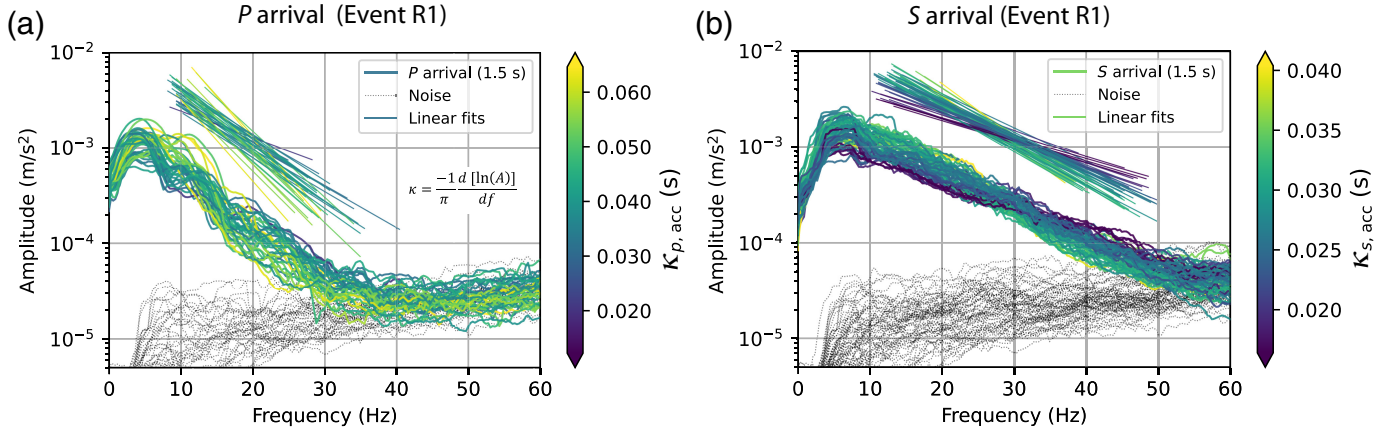
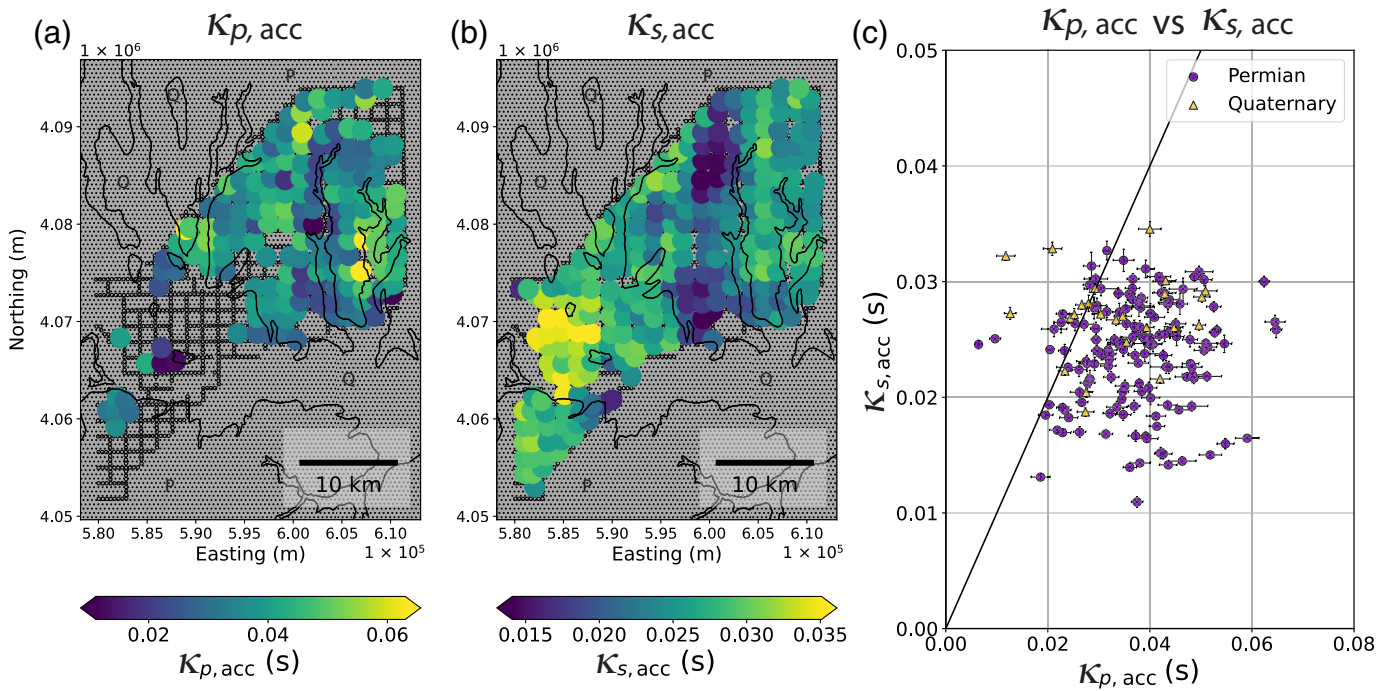


Figure 3. High-frequency spectral decay parameter kappa (κ) measured from the vertical component of the acceleration spectra of regional event R1. (a) P arrival for $\kappa_{p,\text{acc}}$ and (b) S arrival for $\kappa_{s,\text{acc}}$. The spectra are stacked among stations within a subarray of a 2.5 km diameter circle (15–20 stations). The signal spectra (colored) are calculated in a 1.5 s window around the P or S arrivals. The noise spectra (black dotted) are calculated in a 1.5 s window

8 s before the P arrivals. The thin colored lines are linear fits between amplitude (A) and frequency (f) for estimating kappa. We require a minimum frequency bandwidth of 15 Hz. See Figure 2 for the criteria for determining the frequency range. Only one-fourth of the total spectra and fitting are shown (equally spaced across the array) for visualization. The color version of this figure is available only in the electronic edition.



The kappa value consists of a path component ($\kappa_{r,\text{acc}}(r)$) and a site component ($\kappa_{0,\text{acc}}$) (Ktenidou *et al.*, 2015):

$$\kappa_{\text{acc}} \approx \kappa_{r,\text{acc}}(r) + \kappa_{0,\text{acc}}. \quad (6)$$

Here, r represents the epicentral distance. We can obtain the site term after removing the distance-dependent $\kappa_{r,\text{acc}}(r)$. According to Ktenidou *et al.* (2016), a distance of 50–100 km is necessary to observe the κ -distance relation in the central and eastern United States (CEUS), in which the crust has low attenuation. The total epicentral distance (>125 km) is sufficient to resolve $\kappa_{r,\text{acc}}$. However, the distance difference between subarrays is less than 20 km (<20% of the total distance), which is too small to resolve the distance dependence within the array (Fig. S4). We assume the path term is nearly constant across the array and the path term is represented by the minimum κ_{acc} of the three events (i.e., $\kappa_{r,\text{acc}} = \min(\kappa_{\text{acc}})$). This gives $\kappa_{r,p,\text{acc}} = 0.004$ s for P waves and $\kappa_{r,s,\text{acc}} = 0.010$ s for S waves. We estimate the site term $\kappa_{0,\text{acc}}$ by subtracting $\min(\kappa_{\text{acc}})$ from κ_{acc} . The site-dependent kappa $\kappa_{0,p,\text{acc}}$ ranges between 0.002 and 0.060 s (mostly on the Permian rocks), and $\kappa_{0,s,\text{acc}}$ ranges between 0.001 and 0.030 s (Fig. 5). The majority of the Quaternary sites, and many Permian sites, have $\kappa_{0,s,\text{acc}} > 0.015$ s. Note that the range of site-dependent kappa is 3 times the total path-related kappa for S waves and almost 15 times for P waves. The site-related kappa is 10%–75% of the total kappa for S waves and can be more than 90% for P waves.

We examine how the site-dependent $\kappa_{0,s,\text{acc}}$ relates to ground motions at different frequency bands. We calculate the root mean square (rms) amplitudes for S waves for the regional earthquakes. The rms amplitudes are calculated in a 5 s time window starting from 0.5 s before the S arrival (similar to Chang *et al.*, 2023, but with a shorter time window).

Figure 4. High-frequency spectral decay parameter kappa (vertical component): (a) $\kappa_{p,\text{acc}}$ and (b) $\kappa_{s,\text{acc}}$, and (c) their comparisons. The kappa values are the median of regional events R1–R3. In panels (a) and (b), each colored circle represents a subarray consisting of stations within a 2.5 km diameter circle (15–20 stations; small, black, hollow circles). The color ranges exclude the 1% lowest and highest values for visualization. The contours indicate the boundaries of the surficial Quaternary formations (Q) versus the Permian formations (P). The error bars in panel (c) are the standard deviation of the fitting. The spectral decay is mostly site-dependent, with the Quaternary sediments being more attenuating than the Permian rocks. The color version of this figure is available only in the electronic edition.

Figure 6a shows that $\kappa_{0,s,\text{acc}}$ positively correlates with ground motions below 25 Hz and negatively correlates with ground motions above 30 Hz. Hence, a higher $\kappa_{0,s,\text{acc}}$ is both a result of higher amplitudes at lower frequencies and lower amplitudes at higher frequencies. This observation is consistent with the comparison between surface and borehole (2.5 km depth) recordings of earthquake spectra at Cajon Pass, California (Abercrombie and Leary, 1993). The spectrum from their surface station showed relative amplification at lower frequencies and attenuation at higher frequencies. The transition from amplification to attenuation would shift to lower frequencies in regions with higher attenuation. See [Potential impacts of site amplification](#) for more discussions.

We examine how $\kappa_{0,s,\text{acc}}$ measured from the regional events relates to the corner-frequency estimates for the local events in KN20. We select the three of the best recorded local events (L1–L3; Table S2; event L1 is shown in Fig. 1c). In each event, for each subarray, we calculate the median f_c of individual station estimates in KN20. In Figure 6b, $\kappa_{0,s,\text{acc}}$ negatively correlates with the estimated corner frequency in KN20. The

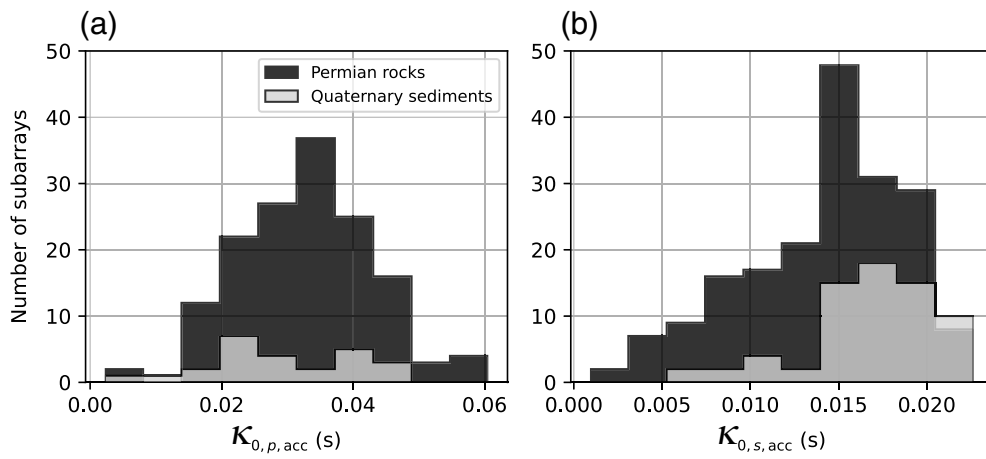


Figure 5. Distribution of the site-dependent kappa estimated (a) for P waves ($\kappa_{0,p,\text{acc}}$) and (b) for S waves ($\kappa_{0,s,\text{acc}}$), determined using the vertical component of the acceleration spectra of regional events R1–R3. Dark color represents sites on Permian rocks, and light color represents those on Quaternary sediments. Note that most Quaternary sites do not have available $\kappa_{0,p,\text{acc}}$ because of the high attenuation. The Quaternary sediments generally have higher $\kappa_{0,s,\text{acc}}$ than the Permian rocks, but the Permian rock sites can also have high attenuation.

correlation between these two independent measurements indicates potential site biases. Our results are consistent with Shearer *et al.* (2024; this special issue). They investigated f_c and model attenuation between different methods for two Ridgecrest

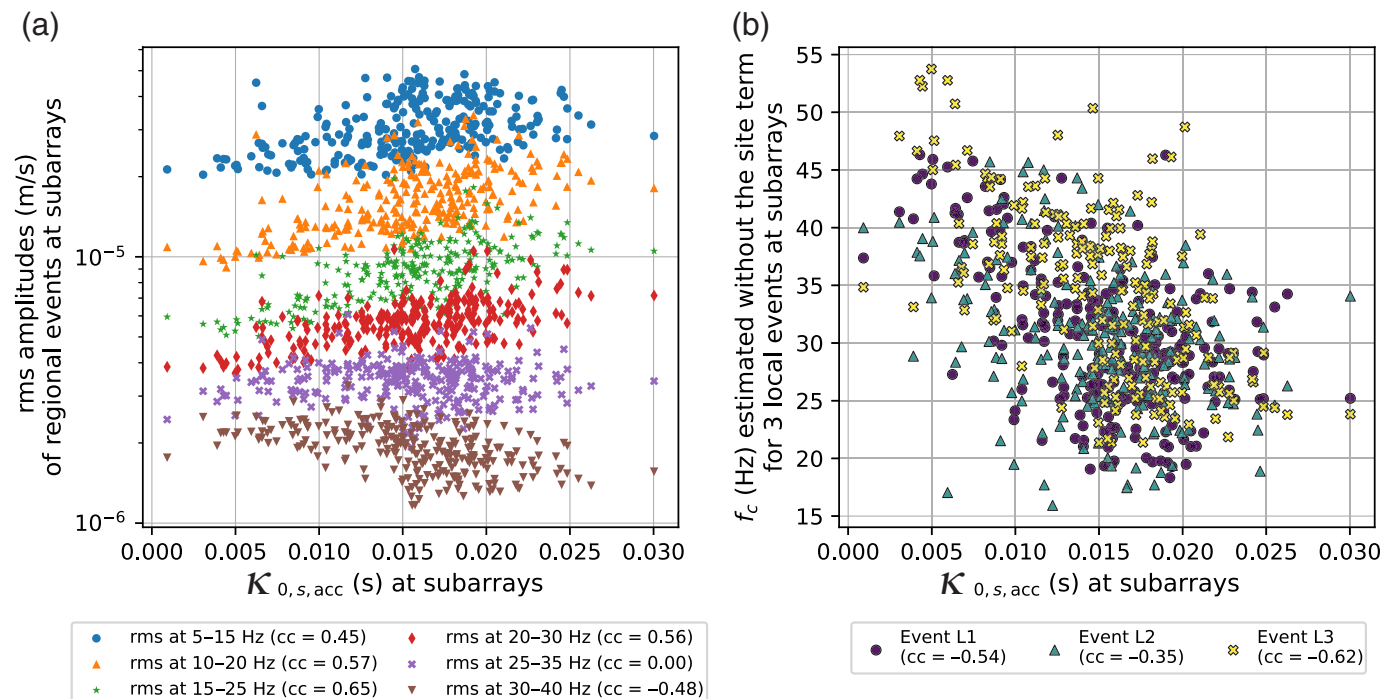


Figure 6. Relationship between site-dependent kappa ($\kappa_{0,s,\text{acc}}$) and (a) median vertical ground motion at different frequencies, and (b) corner-frequency (f_c) measurements of three local events (L1–L3) in KN20. The root mean square (rms) amplitude is in the S -wave window (5 s after the S arrivals), taking the median among the three regional events (R1–R3). Each f_c is the median value

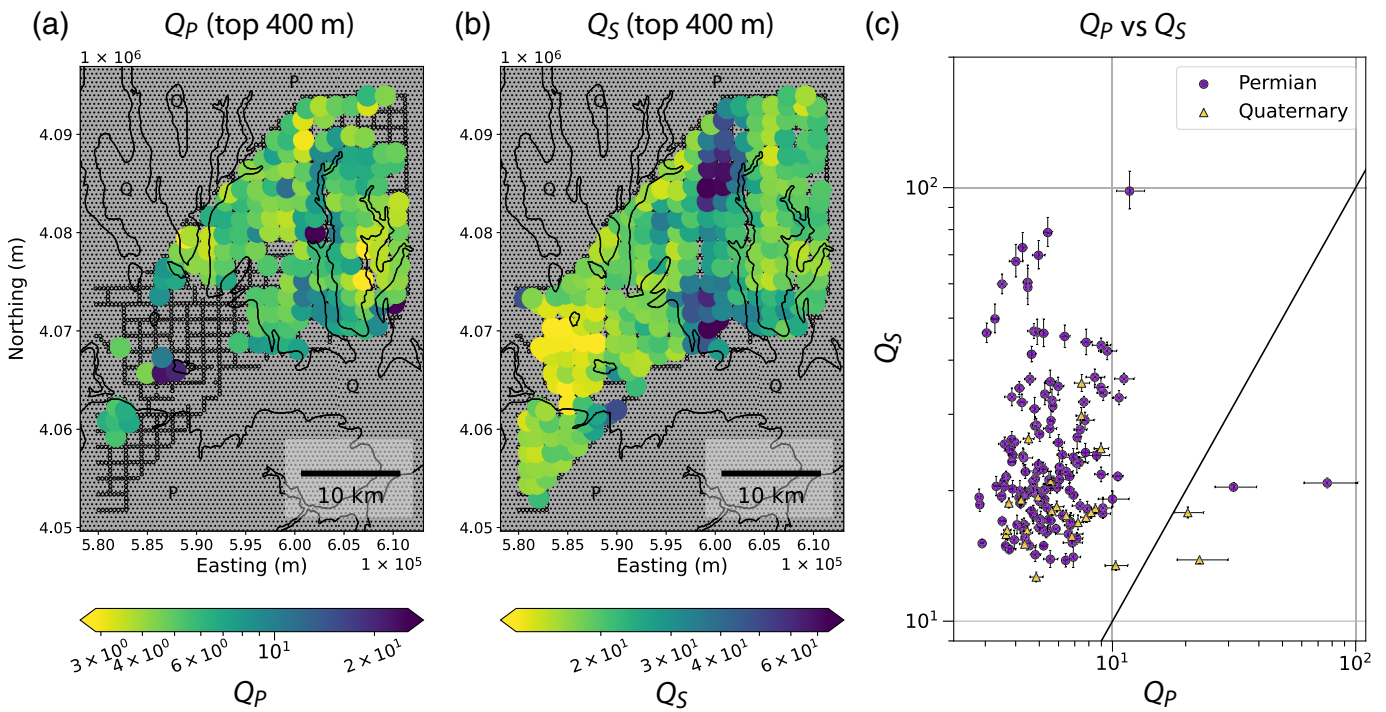
aftershocks. They found methods that use higher kappa tend to have higher f_c results, which suggests trade-offs between kappa and f_c . Here, our kappa is measured independently from the f_c . The fact that sites with a higher kappa tend to get lower f_c suggests biases due to neglecting site effects under the assumption of $\kappa = tt/Q$ in KN20.

If we assume the site-dependent attenuation is primarily occurring in the upper H m, we can convert the site kappa into average estimates of shallow Q using

$$Q = \frac{\sum_{i=0}^{i=N} tt_i}{\kappa_{0,\text{acc}}}, \quad (7)$$

in which N is the number of layers with a total thickness of H , above which the site term primarily occurs. $\sum_{i=0}^{i=N} tt_i$ is the travel time spent in the shallow layers and can be estimated by a velocity model and raytracing. We use the S -wave velocity

among 15–20 station measurements in a subarray. $\kappa_{0,s,\text{acc}}$ is measured on the vertical component. cc is Pearson's cross-correlation coefficient (all nonzero cc have p -values $<5\%$). $\kappa_{0,s,\text{acc}}$ relates to amplification below 25 Hz and attenuation above 25 Hz. Decreasing f_c with higher $\kappa_{0,s,\text{acc}}$ suggests site-effect biases. The color version of this figure is available only in the electronic edition.



models from [Rubinstein et al. \(2018\)](#) (for 1.5 km and deeper) and [Chang et al. \(2024\)](#) (for shallower than 1.5 km) and assume $V_P = 1.78 V_S$ for P-wave velocity ([Catchings, 1999](#)). We estimate the travel time using the TauP module (using the spherical grid) in ObsPy ([Beyreuther et al., 2010](#)). To determine H , we refer to the previous studies in this region. [Chang et al. \(2024\)](#) found rapidly decreasing velocity at the shallower depth with little lateral changes (Figs. S5 and S6). There are roughly four known interfaces that likely relate to the shallow attenuation: (1) a few to tens of meters (shallow Quaternary deposits; [Johnson and Luza, 2008](#)), (2) ~400 m (rapid velocity transitions), (3) ~1.2 km (rapid velocity transitions), and (4) ~2.3 km (basin basement; [Crain and Chang, 2018](#)).

In this way, if we assume $H = 400$ m, Q_P ranges from 3 to 25 with 95% under 10 and Q_S ranges from 10 to 80 with 95% under 45 (Fig. 7). The Quaternary formations have Q_S less than 30 and only a few very-low Q_P (<10) available. If we assume $H = 2$ km (near the total depth of the sedimentary basin), we get $Q_P = 10\text{--}80$ (95% under 30) and $Q_S = 30\text{--}240$ (95% under 140) in the top 2 km. Different assumptions for H shift the range of Q_S but do not significantly alter the pattern (Fig. S7) because the lateral variations of V_S (and therefore variation of travel time in equation 7) are small in the top 2 km. Whether H is 100 m or 2 km, the measured Q_S indicates strong attenuation with considerable variability near the surface. In general, we have $Q_P/Q_S < 1$ (Fig. 7c) as expected for partially saturated rocks ([Toksöz et al., 1979](#); [Hauksson and Shearer, 2006](#)). On the other hand, the Q associated with the path term ($\kappa_{r,\text{acc}}$) is more than 3000 (estimated based on P- and S-wave travel times of ~20 and 40 s, respectively), which is a lot higher compared to the near-surface Q .

Figure 7. Quality factors for (a) P waves (Q_P) and (b) S waves (Q_S) in the top 400 m were derived using $\kappa_{0,\text{acc}}$ (vertical component). (c) Q_P versus Q_S . The Q_P and Q_S are derived from the site spectral decay parameter and the shear-wave velocity structure. The black line in panel (c) is the 1:1 line. Attenuations for P waves are too high on the Quaternary sediments to measure Q_P . $Q_P < 10$ on 95% of the Permian rock sites. 95% of the total sites have $Q_S < 45$. $Q_P/Q_S < 1$ is expected for partially saturated rocks. See the caption of Figure 4 for other features in the figure. The color version of this figure is available only in the electronic edition.

In the next section, we assume Q_S represents site attenuation for both P and S waves for the local events. This is because we need to characterize the high attenuation on the Quaternary sites but not many Quaternary sites have available Q_P . This would lead to a more conservative estimate as Q_P in general is less than Q_S . All investigations are for the vertical component as the LASSO array does not have the horizontal component.

EFFECTS OF IGNORING THE SITE-DEPENDENT SPECTRAL DECAY

To investigate the effect of ignoring site-related attenuation, we generate synthetic displacement spectra and use different assumptions to fit them. We use the source-subarray configuration of local event L1 with the Q -values observed in the previous section. We generate the synthetic spectra using equation (3) with $f_c = 30.0$ Hz, $\gamma = 2$, $n = 2.0$, and an arbitrary low-frequency amplitude level of $\Omega_0 = 10$. The attenuation parameter κ for each subarray is formulated as

$$\kappa = \kappa_{\text{path}} + \kappa_{\text{site}}, \quad (8)$$

$$= \frac{tt - \sum_{i=0}^{i=N} tt_i}{Q_{\text{path}}} + \frac{\sum_{i=0}^{i=N} tt_i}{Q_{\text{site}}}. \quad (9)$$

The first term (κ_{path}) and the second term (κ_{site}) are the path- and site-dependent attenuation. $\sum_{i=0}^{i=N} tt_i$ is the sum of travel time spent in the top $H = 400$ m, and tt is the total travel time from the source to the middle of the subarray. In our configuration, the waves spend less than 20% of time in the top 400 m. Q_{site} and Q_{path} are the site- and path-specific Q values. We calculate the ray travel time using Pykonal (using the Cartesian grid; White *et al.*, 2020). The velocity structure is from Chang *et al.* (2024) for the top 1.5 km and Rubinsteine *et al.* (2018) for below 1.5 km, and we assume $V_p = 1.78 V_s$. We generate synthetic spectra using either P -wave velocity or S -wave velocity using $Q_{\text{site}} = Q_s$ obtained from kappa of regional earthquakes.

We assume $Q_{\text{path}} = 1000$, which is a rough assumption that is chosen between Singh and Herrmann (1983) ($Q \approx 850$) and Benz *et al.* (1997) ($Q \approx 1300$) for this region. We also try $Q_{\text{path}} = 300$ (Levandowski *et al.*, 2021) and find that the results would not change because these values are all relatively high compared to Q_{site} . Note that the usage of a single Q_{path} without a source-depth dependence can be an oversimplification for real earthquakes, but we will focus on the difference in sites and will not address potential issues due to difference in Q_{path} here as the earthquakes are all relatively shallow (1.5–5.5 km; see Other potential factors).

We fit the synthetic spectra with different attenuation models and source constraints (Table 1) in a series of tests to explore the trade-offs between source and path parameters. The travel times are known parameters from raytracing, and the velocity model (either V_p or V_s). Synthetic test 1 is a benchmark that includes the parameters used to generate the original synthetics (equations 3 and 9). We allow both f_c and Q_{site} to vary and fix $\gamma = 2$. We perform a grid search to find the combination of Q_{path} and n that gives the overall best fit for all subarrays. We successfully recover $f_c = 30.0$ Hz and Q_{site} at all subarrays for these ideal spectra.

In synthetic tests 2–5, we ignore site effects with different source constraints (Table 1) when fitting the synthetic spectra

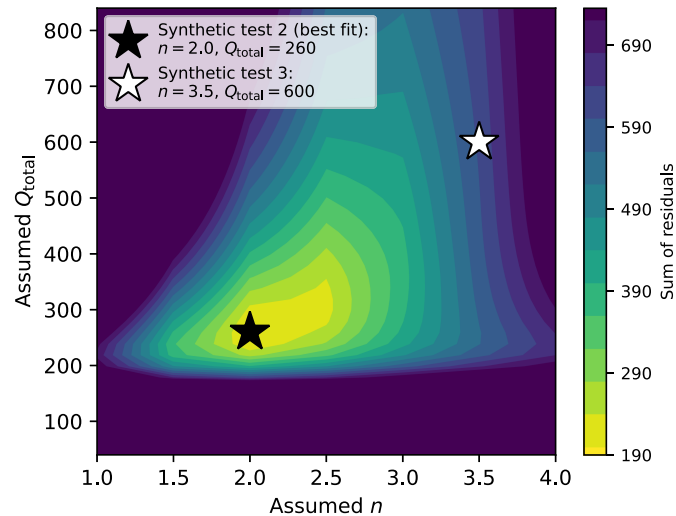


Figure 8. Trade-offs between attenuation and source spectral fall-off parameter n when we attempt to use only travel-time-dependent attenuation ($\kappa = \kappa_{\text{path}} = \text{travel time}/Q_{\text{total}}$) to fit synthetic spectra that include site attenuation ($\kappa = \kappa_{\text{path}} + \kappa_{\text{site}}$). Q_{total} is the overall quality factor assumed to characterize the attenuation. The colors indicate the sum of residuals from fitting the synthetic spectra at all subarrays. We perform synthetic test 2 using the overall best fit at the black star and test 3 using the combination at the white star (the best fit for real data in KN20). The color version of this figure is available only in the electronic edition.

(generated including the site term). We ignore the site term by assuming $\kappa_{\text{site}} = 0$ in equation (9), and so the path Q equals to the total Q along the path of propagation: $Q_{\text{path}} = Q_{\text{total}}$. In test 2, we allow Q_{total} , n , and f_c to vary. A grid search finds a combination of $Q_{\text{total}} = 260$ and $n = 2.0$ gives the overall best fit (black star in Fig. 8). This solution does not change if we use only Permian (higher Q_{site}) or Quaternary sites (lower Q_{site}). The map of residuals shows the trade-off between Q_{total} and n as spectral fall-off parameter n tries to compensate for the unmodeled attenuation in the spectra. In test 3, we assume a combination of higher $Q_{\text{total}} = 600$ and higher $n = 3.5$ (white star in Fig. 8), which is the best combination found for the actual data of event L1 in KN20 and solve for f_c .

TABLE 1
Fitting Conditions of KN20 and the Synthetic Tests

Name	V_p or V_s	Attenuation Model	Fixed Variables	Dependent Variables	$\frac{\text{Apparent } f_c}{\text{True } f_c}$
KN20	V_p	$\kappa = \kappa_{\text{path}}$	$Q_{\text{total}} = 600, n = 3.5$ (best fit)	$Q_{\text{total}}, n, \gamma, f_c$?
Synthetic test 1	V_p	$\kappa = \kappa_{\text{path}} + \kappa_{\text{site}}$	$Q_{\text{path}} = 350, n = 2.0$ (best fit)	$Q_{\text{path}}, Q_{\text{site}}, n, f_c$	100%
Synthetic test 2	V_p	$\kappa = \kappa_{\text{path}}$	$Q_{\text{total}} = 260, n = 2.0$ (best fit)	Q_{total}, n, f_c	96%
Synthetic test 3	V_p	$\kappa = \kappa_{\text{path}}$	$Q_{\text{total}} = 600, n = 3.5$	f_c	93%
Synthetic test 4	V_s	$\kappa = \kappa_{\text{path}}$	$Q_{\text{total}} = 280, n = 2.5$ (best fit)	Q_{total}, n, f_c	93%
Synthetic test 5	V_s	$\kappa = \kappa_{\text{path}}$	$Q_{\text{total}} = 600, n = 3.5$	f_c	68%

The synthetic spectra are generated using either P -wave velocity (V_p) or S -wave velocity ($V_s = V_p/1.78$), and a true $f_c = 30$ Hz. V_p and V_s are known parameters in the fitting. Test 1 is a benchmark that uses the same attenuation model to fit the spectra. Tests 2–5 use a model without the site term ($\kappa_{\text{site}} = 0$). Apparent f_c is the test's median of good measurements (<5% uncertainty). "?" means unknown.

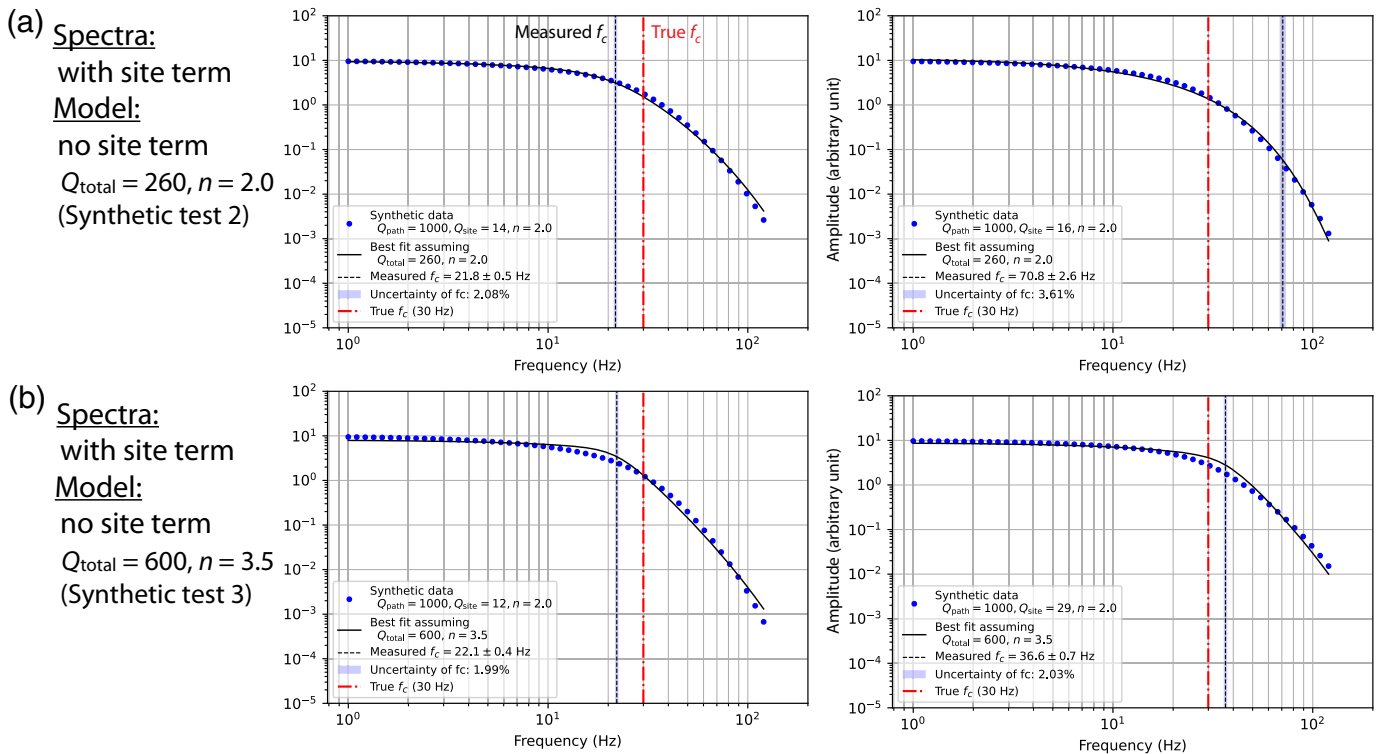


Figure 9 shows the spectral fitting examples in the second and the third synthetic tests where we ignore the site terms. The models seem to fit well with small uncertainties. However, the measured f_c is significantly off from the true $f_c = 30$ Hz. Note that with some narrowband amplification (such as the small peaks between 10 and 20 Hz seen in the observed spectra shown in Fig. 2a), the grid search might find $Q_{\text{total}} = 600$ and $n = 3.5$ in Figure 9b to fit the spectra better.

Figure 10 shows the highly variable f_c measurements of all subarrays obtained in the sequence of synthetic tests (Table 1). These measurements have fairly good fits with uncertainty less than 5%. However, the apparent f_c scatter across 15–90 Hz among subarrays is due to the oversimplified attenuation model. Because the actual attenuation involves both the site quality factor (Q_{site}) and travel time (equation 9), the measured f_c correlates with the actual Q_{site} (i.e., Q_S) and the hypocentral distance (Fig. 10a). However, the large scattering can mask the correlations. When assuming another set of Q_{total} and n , the apparent relation between f_c and Q_S and the hypocentral distance changes (Fig. 10b). The correlation between f_c and hypocentral distance may not be obvious.

Notice that the median f_c deviates from the true f_c . The deviation of the median f_c increases when the assumed n is higher than the true n (Fig. 10b,d) because a varying n contributes to the parameter trade-off. The deviation of the median f_c can be severe with a low-velocity structure—in this case, V_S (Fig. 10c,d), which is 1.78 times lower than V_P . This is because longer travel times increase the range of kappa (equation 4), which increases the biases. Having a lower Q structure

Figure 9. Models with different attenuation assumptions fit the synthetic spectra well while the corner-frequency estimates are off. Synthetic tests (a) 2 and (b) 3 use models (dashed curves) without site attenuation ($\kappa = \kappa_{\text{path}}$) to fit synthetics (points) generated including site attenuation ($\kappa = \kappa_{\text{path}} + \kappa_{\text{site}}$). The apparent f_c (vertical dashed lines) can deviate significantly from the true $f_c = 30$ Hz (vertical, dashed dotted lines) with small fitting uncertainties (shades around the dashed lines). The color version of this figure is available only in the electronic edition.

would have the same effect of increasing the range of kappa and the site-effect biases.

Now, we compare the real data of event L1 with the synthetic test results. KN20 used a similar assumption to our third synthetic test. They assumed κ is entirely travel-time dependent and found $Q_{\text{total}} = 600$ and $n = 3.5$ fit the overall data the best, possibly due to site amplifications on the Quaternary sites. We observe similar site and distance dependence in their f_c measurements comparing Figure 10e with 10b. The resemblance suggests trade-offs between f_c and Q_{site} , an overestimated n , and possibly a biased f_c overall for this event due to site effects. Other local events also exhibit site dependence (Figs. S8 and S9).

REDETERMINING SOURCE PARAMETERS CONSIDERING THE SITE ATTENUATION

We re-estimate the source parameters using P arrivals for all local events considering observed spectral decays. Different from the single-spectra approach in KN20 that assumed $\kappa = \kappa_{\text{path}}$, we include site attenuation with $\kappa = \kappa_{\text{path}} + \kappa_{\text{site}}$. In addition, we implement site-selection criteria to include

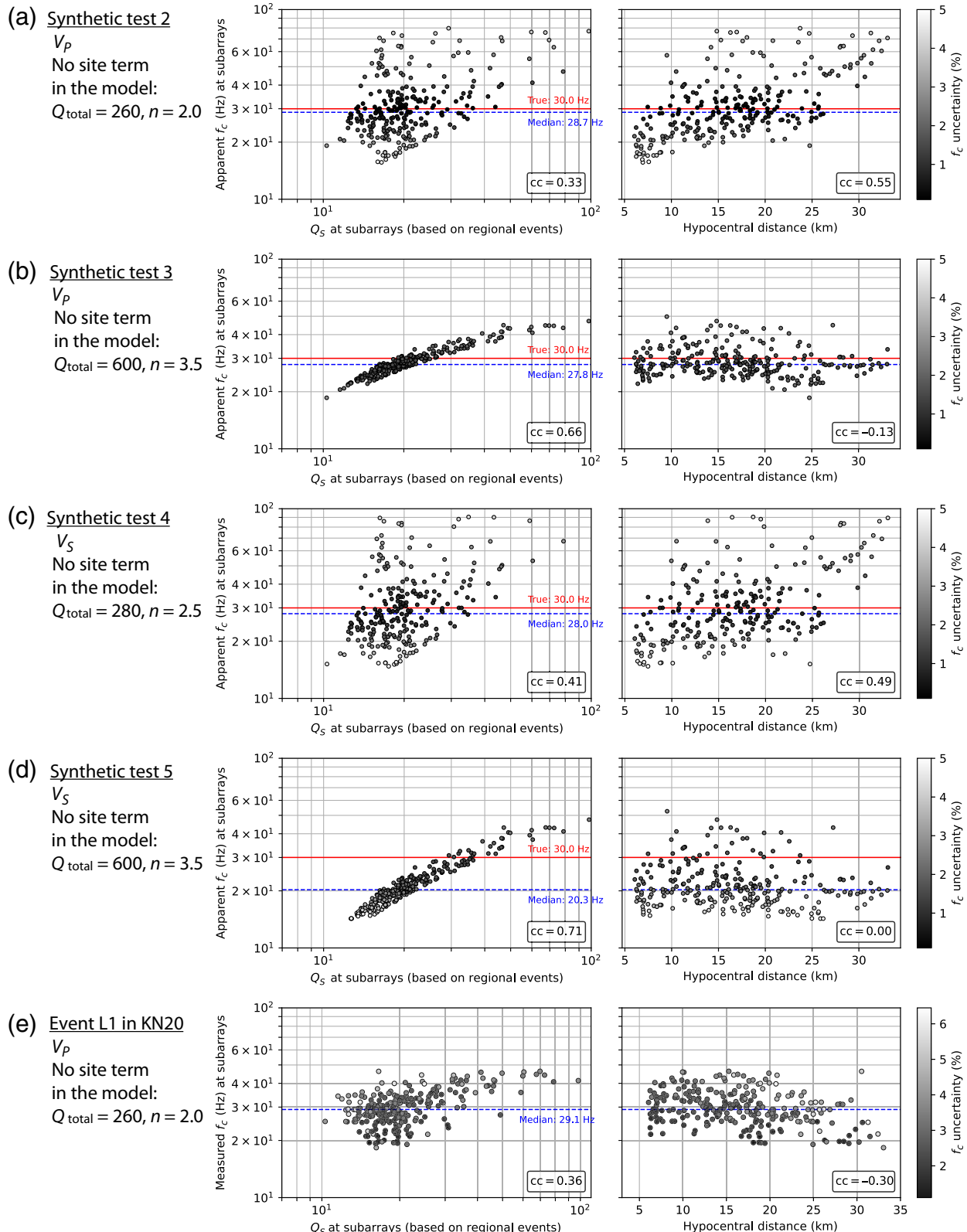
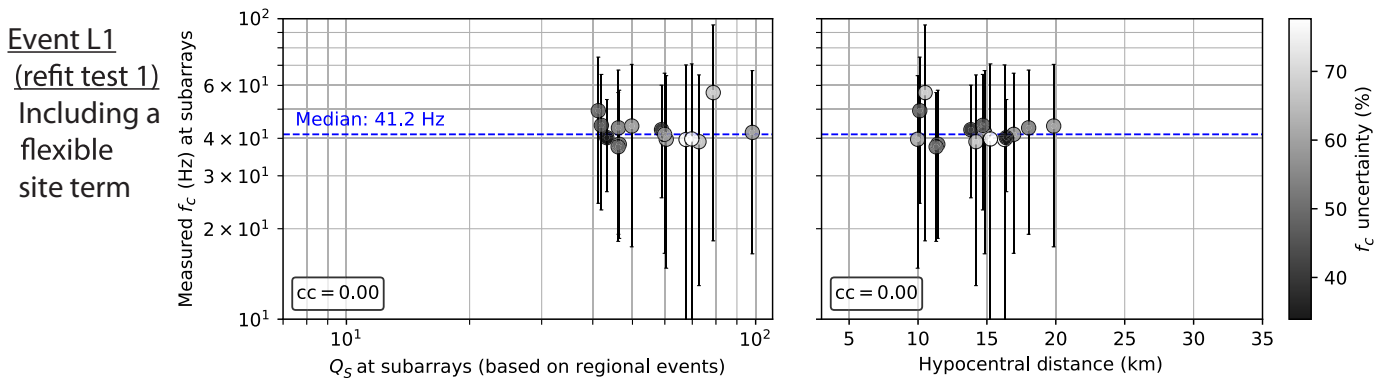


Figure 10. Relationship between apparent corner-frequency (f_c) and actual site attenuation (Q_s , left) and hypocentral distance (right) when the f_c is derived ignoring site attenuation. Synthetic tests 2–5 (a–d) assume $\kappa = \kappa_{\text{path}}$ with travel-time-dependent attenuation to fit the synthetic spectra generated including site attenuation ($\kappa = \kappa_{\text{path}} + \kappa_{\text{site}}$). The median of the apparent f_c (horizontal dashed lines) deviates from the true f_c (30 Hz, horizontal solid lines). The deviation can be severe when κ increases (e.g., with lower S-wave

velocity like in panel (d), or equivalently, with lower Q) and the source constraint n joins the trade-offs ($n = 3.5$, larger than the true value of 2). (e) The measured f_c from actual data of event L1 in KN20. The color scales indicate fitting uncertainty ((standard deviation of f_c)/ f_c × 100%). cc is Pearson's cross-correlation coefficient (all nonzero cc have p -values <5%). The color version of this figure is available only in the electronic edition.



only Permian sites with a higher apparent Q_S or Q_P (from the regional events).

In the first test (refit test 1; Table 2), we let the site-dependent Q_{site} be flexible in the spectral fitting. We

1. Determine f_c and Q_{site} by fitting stacked P -wave spectra (equation 3) while fixing $\gamma = 2$ and $n = 2.0$.
2. Determine Q_{path} by grid searching the Q_{path} that gives the lowest misfit in 1 for event L1 (recorded by the most number of stations). We find $Q_{\text{path}} = 300$, which is applied to all other events.

Refit test 1 uses only Permian sites with Q_S higher than the 92nd percentile ($Q_S > 37$). The travel times spent in the top 0.4 km (associated with Q_{site}) and below (associated with Q_{path}) are calculated using the Eikonal equations (White *et al.*, 2020). The $Q_{\text{path}} = 300$ we obtain is consistent with Levandowski *et al.* (2021) ($Q \approx 250$) but lower than $Q \approx 850$ in Singh and Herrmann (1983) for northern Oklahoma and $Q \approx 1300$ in Benz *et al.* (1997) for the CEUS. Our Q_{path} should be higher than their Q because Q_{path} already excluded Q_{site} . We use a 0.8 s window around the P arrivals to calculate the displacement spectra. Data treatment before spectral fitting includes applying pointwise quality control to discard data points with SNR less than nine, resampling the spectra into a constant interval on the log-frequency scale, and stacking the resampled spectra in each subarray. See Text S2 for details.

Figure 11 shows the recalculated f_c for event L1 in refit test 1. We plot the f_c results with fitting uncertainty less than 100%. There is no correlation between f_c and Q_{site} or f_c and

Figure 11. Correlation between corner frequency (f_c) and the actual Q_{site} (i.e., Q_S ; left) and hypocentral distance (right) decreases after including a flexible site term for event L1 in refit test 1. Compared to Figure 10e (we plot in the same x-scale for comparison here), the site- and distance-dependent correlations are removed in refit test 1 with a higher median f_c for event L1. The error bars indicate the standard deviation of the least-square fitting. The color scales indicate uncertainty. The horizontal dashed lines are the median f_c . Each point represents a subarray with 15–20 stations within a 2.5 km diameter circle. See the caption of Figure 10 for other features. The color version of this figure is available only in the electronic edition.

hypocentral distance in Figure 11 compared to the results in KN20 (Fig. 10e). The other two events (L2, L3; Figs. S8 and S9) still exhibit some correlations as the models are still simplified. Despite the large fitting uncertainty, the f_c results among subarrays are consistent with a higher median f_c (41.2 Hz) than that in KN20 (29.1 Hz).

We further refine the results in refit test 1 by requiring the minimum fitting uncertainty for f_c to be less than 20%. Figure 12 shows the Q_{site} fitting results, taking the median among available local events. The spectral fitting yields varying Q_{site} with many of them much lower than Q_{path} (300). However, the Q_{site} determined by spectral fitting does not correlate with Q_P and Q_S determined by kappa measured from the large distant events. The lack of correlation suggests that we do not have a good resolution to determine the spatial distribution of Q_{site} in the source spectra fitting for local events.

Although we might not have a good resolution to resolve Q_{site} in source spectra fitting, by including Q_{site} , we can reduce the

TABLE 2
Fitting Conditions for Determining Source Parameters of Large-n Seismic Survey in Oklahoma (LASSO) Local Events

Name	Attenuation Model	Site Selection Criteria	Fixed Variables	Dependent Variables
KN20	$\kappa = \kappa_{\text{path}}$	Permian + Quaternary sites	–	$Q_{\text{total}}, n, \gamma, f_c$
Refit test 1	$\kappa = \kappa_{\text{path}} + \kappa_{\text{site}}$	Permian sites with $Q_S > 37$	$n = 2.0, \gamma = 2$	$Q_{\text{path}}, f_c, Q_{\text{site}}$
Refit test 2	$\kappa = \kappa_{\text{path}} + \kappa_{\text{site}}$	Permian sites with $Q_P > 9$	$n = 2.0, \gamma = 2, Q_{\text{site}} = Q_P$	Q_{path}, f_c

The refit tests 1 and 2 include an additional site term (κ_{site}) compared to KN20, which assumed a travel-time-dependent attenuation. In the column of the dependent variables, n , γ , f_c , and Q_{site} are determined by fitting stacked spectra, and Q_{total} and Q_{path} are determined by grid searching for the lowest misfit.

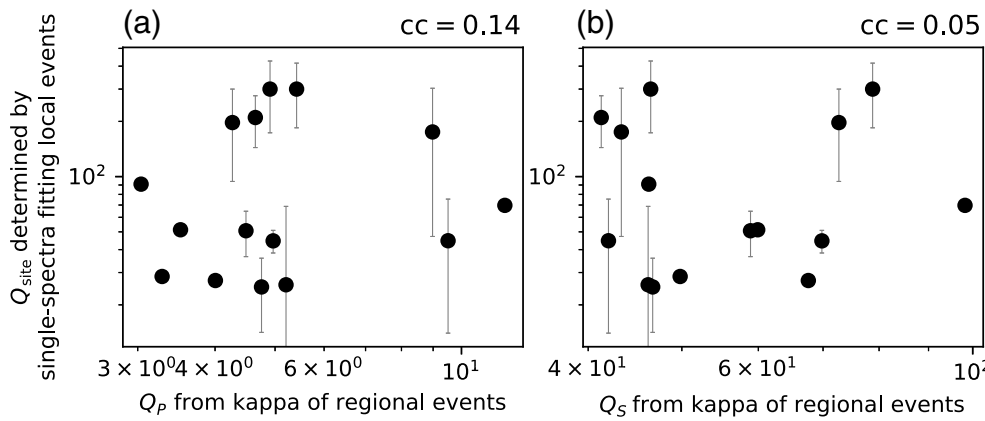


Figure 12. Site-dependent quality factor (Q_{site}) determined by spectral fitting local events (refit test 1) versus (a) Q_P and (b) Q_S determined from the kappa measured from the acceleration spectra of regional events. Q_{site} is the median of results from all local events with error bars indicating the standard deviation. Q_{site} are generally much lower than $Q_{\text{path}} = 300$. cc is Pearson's cross-correlation coefficient. The lack of correlations indicates that source spectra fitting of local events might not have a good resolution for the spatial distribution of Q_{site} .

biases that come from parameter trade-offs. We compare the magnitude and stress drop of refit test 1 with KN20. We calculate the stress drop using equation (2), assuming β based on source depth and the velocity structure (Rubinstein *et al.*, 2018), the same $k = 0.38$, the same M_0 in KN20, and moment magnitude (M_w) based on Hanks and Kanamori (1979). The single-spectra results in KN20 show smaller events deviating from the lines of constant stress drops (Fig. 13a), whereas the results in refit test 1 do not exhibit obvious scaling relations between M_w and stress drop (Fig. 13b). The increasing stress drop with increasing magnitude in the single-spectra fitting results in KN20 is likely associated with site effects, where small events typically with higher corner frequency are more susceptible to attenuation-related trade-offs. Furthermore, the colors in Figure 13a show that

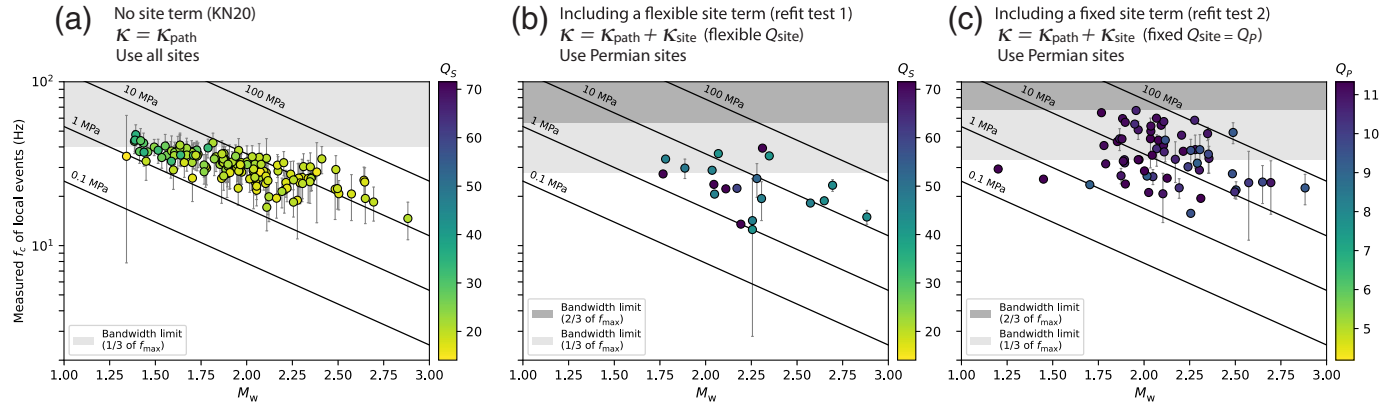


Figure 13. Relations between stress drop (solid straight lines) and moment magnitude (M_w) when (a) not including the site term (KN20), (b) including a flexible site term (refit test 1), and (c) including a fixed site term (refit test 2). Each dot is the median of an event (among subarrays) with error bars indicating the standard deviation of corner frequency (f_c). The colors indicate the average site attenuation (Q_S or Q_P from regional events) of subarrays that participate in the measurements. We only used the higher Q_S

and Q_P sites in panels (b) and (c) (the color bars show the range of average Q for sites used in KN20, excluding the highest 20% for visualization). The solid lines are constant stress drops at 0.1, 1, 10, and 100 MPa. The shades indicate approximate upper bandwidth limits defined as one and two-thirds of the maximum available frequency (f_{max}) of the stacked spectra at subarrays (which are different between the two refit tests). The color version of this figure is available only in the electronic edition.

We conduct a second test (refit test 2; Table 2) that assumes Q_{site} is Q_P determined by the acceleration spectra of regional events. Here is how we determine the parameters:

1. Determine f_c by fitting stacked P -wave spectra (equation 3) while fixing $\gamma = 2$, $n = 2.0$, and $Q_{\text{site}} = Q_P$ (from the regional events).
2. Determine Q_{path} by grid-searching the Q_{path} that gives a lowest misfit in 1. For event L1. We find Q_{path} to be very large and use $Q_{\text{path}} = 99,999$ for all events.

Refit test 2 uses only Permian sites with Q_P higher than the 92nd percentile ($Q_P > 9$). We require an uncertainty of f_c to be less than 20% and calculate the moment magnitudes and stress drops (Fig. 13c). The number of results increases compared to the first test because fixing Q_{site} reduces the degree of freedom, which reduces the uncertainty. The source parameters still do not exhibit an obvious magnitude–stress-drop scaling relation in the second test. The stress drops (median $\Delta\sigma = 16$ MPa) are in general higher than KN20 (4.4 MPa) and refit test 1 (4.3 MPa). This suggests possibly higher actual stress drops. Or, this can also

result from higher P -wave spectral decays for large distant events (where our Q_p estimates are from) than those for the small local events (the actual Q_p), which causes higher apparent corner frequencies.

DISCUSSIONS

Highly attenuating shallow layers with large site dependence

The acceleration spectra of regional earthquakes reveal that attenuation across the area of LASSO is highly site dependent and mainly occurs at the near surface. Despite that the earthquakes are more than 125 km away, 10%–75% of the total kappa is site related for S waves and can be more than 90% for P waves. Abercrombie (1997) found that 90% of attenuation happens in the top 3 km for earthquakes within 15 km at Cajon Pass, California. Here, the epicentral distances are nine times larger, and the site attenuation can still dominate. The surface Quaternary sediments tend to have higher spectral decays, but the Permian rocks can have a high spectral decay as well (Fig. 5).

We find $Q_p = 3\text{--}25$ (mainly on the Permian sites; most Q_p are below 10) and $Q_s = 10\text{--}80$ (on both Quaternary and Permian sites; most Q_s are below 45) in the upper 400 m, and $Q_p = 10\text{--}80$ (most are below 30) and $Q_s = 30\text{--}240$ in the upper 2 km (Fig. 7; most are below 140). The Q -values are approximately within the same range of previous borehole studies in California (Jongmans and Malin, 1995; Abercrombie, 1998) and Switzerland (Bethmann *et al.*, 2012). In comparison, the Q of the deep structure (derived from our regional events with hypocenters at 4–6 km depth, 125 km away) is much higher ($Q > 3000$). These observations are consistent with the tectonic and geological environment. The central United States is in the intraplate stable tectonic regime with soft sediments overlying stiff formations (Johnson and Luza, 2008). Young alluviums are deposited on the post-glacier land, creating local large site effects with a flat topography. Our results can likely extend to much of the central United States with similar geological conditions.

Both the site spectral decay and Q -values indicate higher attenuation for P waves than for S waves. Bethmann *et al.* (2012) also found $Q_p/Q_s \leq 1$ in Switzerland, whereas the California studies (Jongmans and Malin, 1995; Abercrombie, 1998) have $Q_p/Q_s \geq 1$. Variations in Q_p/Q_s can be affected by water contents. Partial saturation tends to have $Q_p/Q_s < 1$, whereas complete saturation tends to have $Q_p/Q_s > 1$ (Winkler and Nur, 1982; Clouser and Langston, 1991; Parolai *et al.*, 2022). We do not further investigate the difference between Q_p and Q_s in this study.

There are some limitations on the Q -values derived from kappa in this study. First, our Q_p and Q_s are lower bound because the shallow velocity is likely lower. The 3D velocity model we used to derive Q lacks good resolution in the upper 50 m. Local average shear-wave velocity in the top 30 m (V_{S30}) is

about 400 m/s (Zalachoris *et al.*, 2017), which is much lower than the $V_S > 900$ m/s at 50 m depth in our velocity model (Fig. S5). The potentially underestimated travel times and Q are less than 5% (for $H \geq 400$ m; equation 7). Second, we do not consider potential broadband amplification (e.g., Boore and Joyner, 1997; Campbell and Bozorgnia, 2014), the apparent Q might be higher at stiff sites and lower at soft sites than the actual values. The apparent Q is sufficient for our purpose of understanding potential site effects for source parameter estimation.

Implications of shallow attenuation on spectral fitting

Under this attenuation structure, assuming a dominantly travel-time-dependent attenuation in Brune's model would cause the apparent corner frequency to vary from site to site and bias overall measurements, the spectral fitting appears good but the f_c deviates from the true value (Fig. 9). The f_c correlates with site attenuation with large scattering from one subarray to another (Figs. 6b and 10). Some studies used the relation between f_c and hypocentral distance to examine uncorrected attenuation (e.g., fig. 13 in Bindi *et al.*, 2020). However, the apparent relation between f_c and distances can be unobvious depending on model assumptions (Fig. 10). A lack of correlation between f_c and distance (or travel time) does not suggest little influence of site effects. The apparent n -values tend to be larger to compensate for the unmodeled site attenuation as both are independent of the total travel time.

Methods to reduce site-effect-related bias and uncertainty

We demonstrate that by adding a site-attenuation term (κ_{site}), restricting spectral fitting to sites on stiffer formations (Permian rocks with higher Q), and implementing the source constraint (fixing n), we can significantly reduce the apparent scaling relation between M_w and stress drop (Fig. 13). The spectral ratio approach is also effective in removing the site effects. Source parameters estimated using the spectral ratio approach do not exhibit an apparent M_w -stress-drop scaling relation (Kemna *et al.*, 2020) or correlations with site conditions (Chang *et al.*, 2023). However, the spectral ratio methods involve other uncertainties (Abercrombie, 2015), and the limited EGF availability for small events can introduce other selection biases. We also attempted to derive nonparametric site response spectra for correction using regional earthquakes. However, because the regional earthquakes have limited SNR above 30 Hz due to attenuation (Fig. S10), we could not get reliable f_c measurements from the corrected spectra.

Chang *et al.* (2023) attempted to correct site effects in the source parameter measurements by removing a linear trend between site amplification and f_c and M_0 . However, their trend removal is based on the median of station-wise measurements in individual events. Such median-based correction underestimates the event-wise bias due to site effects because the median

can deviate from the true value (Fig. 10). On the other hand, one might attempt to find a site-specific scaling factor to correct f_c . However, because the scattering and biases relate not only to the site condition (Q_{site}) but also to the source-receiver configuration and the fitting assumptions, finding a site-specific correction without considering the configuration and the modeling assumption is impossible. Depending on the fitting assumptions, the apparent f_c can have different apparent relations with site conditions and distance. Once the measurements are made, correcting the measurements is not easier than redoing the fitting under a more adequate assumption.

Potential impacts of site amplification

We use the site-dependent spectral decay ($\kappa_{0,\text{acc}}$) from large events to estimate that of local small events. The spectral decay parameter could contain both attenuation and broadband amplification (Boore and Joyner, 1997). We do avoid local strong resonance by averaging spectra and measuring using wide (>15 Hz) and carefully selected frequency bands (Fig. 2). Still, sites on the Quaternary formations tend to have elevated amplitudes under 25 Hz (Fig. S10). Hence, the Q_P and Q_S estimated from the spectral decay are apparent values. In refit test 2, assuming the same Q_P estimated from large regional events for the small local events yields generally higher corner frequencies and stress drops compared to refit test 1. The stress drops are still within the range that agrees with previous studies (Huang et al., 2017). However, the apparent higher f_c might indicate that the observed spectra of small local events have higher apparent Q_P compared to the large regional events, possibly due to less broadband amplification at lower frequencies for the small local events, if other parameters (e.g., n) are the same for these earthquakes.

Although we try to minimize the impact of local strong resonances, a consistently small amplitude bulge can still affect the single spectral fitting, given how close a false model with a biased f_c can resemble the spectra (Fig. 9). Chang et al. (2023) found that ground motions of regional events correlate with f_c in KN20. The advantage of spectral ratio methods, if available, is to take care of the general site and path effects. Otherwise, the site and path effects need to be carefully considered. The unmodeled amplification might cause a higher apparent spectral fall-off rate (n), which if used, would participate in the trade-off and result in large biases in f_c (Fig. 10).

Other potential factors

There is a simplification in our attenuation model, which is the usage of a single path-dependent attenuation Q_{path} in equation (9). In reality, because of the Earth's layered structure, for two earthquakes with the same hypocentral distance, the one directly beneath the station, and thus at a deeper depth, can experience very different attenuation compared to the one at shallower depth. Using the same Q_{path} to characterize both earthquakes causes an increasing stress drop

with source depth (Abercrombie et al., 2021). Baltay et al. (2024) observed that stress drops estimated without considering source-depth-dependent attenuation exhibit a stronger correlation with source depths, in which attenuation likely plays a role. In this study, the depths of local earthquakes are all relatively shallow (1.5–5.5 km), and the ray paths to most of the stations spend significant time traveling in nearly horizontal layers; hence, a purely travel-time-dependent Q_{path} may be sufficient. However, we note that a depth-dependent Q_{path} is required when analyzing earthquakes with greater depths.

Another source of uncertainty comes from source complexity. Some studies observed evidence of complicated source ruptures for microearthquakes at LASSO (Trugman et al., 2021; Pennington et al., 2022; Chang et al., 2023). Fitting complex source spectra with a simple Brune's or a spectral ratio model might also introduce misfit-related uncertainties.

CONCLUSION

We measure the high-frequency spectral decay parameter kappa (κ_{acc}) using the acceleration spectra of regional earthquakes (with moment magnitudes of 3.6–3.7) to investigate shallow attenuation at the LASSO. The dense surface station coverage allows us to stack in multiple subarrays to improve the stability of the measurements while maintaining a high spatial resolution. 10%–75% of the total kappa is site-dependent for S waves and can be more than 90% for P waves, even for events that are over 125 km away. The range of site-related kappa is much larger than the total path-related kappa across the 25 km × 32 km area of the array. The corner frequency (f_c) estimated using the single-spectra approach in Kemna et al. (2020) (denoted as KN20) negatively correlates with the site-dependent kappa (Fig. 6b), suggesting influences of site effects.

We derived the apparent attenuation quality factor (Q) for P and S waves using kappa. The Q values decrease rapidly at shallower depths. In the top 2 km, Q_S ranges from 30 to 240 (95% are below 140), and in the top 400 m, Q_S ranges from 10 to 80 (95% are below 45). The Quaternary sediments tend to have higher attenuation (95% have $Q_S < 30$ in the top 400 m), but the Permian rocks can be highly attenuating as well (Figs. 5 and 7). 95% of the sites have Q_P lower than 10 in the top 400 m.

We investigate the impact of ignoring site-dependent spectral decay when fitting with Brune's source model for local micro-earthquakes ($1.3 < M_w < 3.0$). Using synthetic spectra, we demonstrate that mixing stations with different site conditions while ignoring site-specific attenuation results in large interstation variation in apparent f_c and serious biases between events (Fig. 10). The impact is more severe if the range of site-dependent kappa increases, such as in lower velocity structures or with higher site-dependent attenuations. The spectral fall-off parameter n tends to be higher than the actual value to accommodate the site-dependent attenuation, which then worsens the trade-offs and can cause serious bias in f_c . The biased measurements

may have little or no apparent correlation with distance depending on fitting assumptions. The fitting uncertainty fails to account for the scattering and bias because of the nonuniqueness of the model (Fig. 9).

By adding a site-dependent attenuation term using only sites on stiff formations and fixing n , we show that a relation of increasing stress drop with increasing magnitude in the previous study is likely an artifact due to trade-offs between f_c , n , and attenuation. This study demonstrates the importance of considering near-surface attenuation even within a simple, flat, small region. Using a small number of stations with controlled site conditions is more precise and accurate than having a large number of stations with uncontrolled site conditions.

DATA AND RESOURCES

The authors use ObsPy (Beyreuther *et al.*, 2010) for earthquake data processing. The authors use the TauP module in ObsPy to calculate travel times for regional events. All spectral fittings in the Shallow Attenuation Across the LASSO Array and the Redetermining Source Parameters Considering the Site Attenuation sections are done using LMFIT (Newville *et al.*, 2016). We use PyKonal (White *et al.*, 2020) to calculate travel times for all local events. All data used in this article came from published sources listed in the references. The supplemental material includes descriptions of data processing, supporting figures, and tables that contain information on the earthquakes analyzed.

DECLARATION OF COMPETING INTERESTS

The authors acknowledge that there are no conflicts of interest recorded.

ACKNOWLEDGMENTS

The authors thank Annemarie S. Baltay, Gail M. Atkinson, and an anonymous reviewer for providing constructive feedback that significantly improves the article. The authors also thank Olga-Joan Ktenidou for the helpful discussion. This research was supported by the U.S. Geological Survey under Grant G20AP00022, G20AP00023, G22AP00012, and G22AP00035 to the Massachusetts Institute of Technology and Boston University. Nori Nakata is partially supported by the U.S. Department of Energy under Award Number DE-AC02-05CH11231 for this study. Hilary Chang was partially funded by The MathWorks Science Fellowship.

REFERENCES

- Abercrombie, R. (1998). A Summary of Attenuation Measurements from Borehole Recordings of Earthquakes: The 10 Hz Transition Problem, *Pure Appl. Geophys.* **153**, 475–487, doi: [10.1007/s000240050204](https://doi.org/10.1007/s000240050204).
- Abercrombie, R., and P. Leary (1993). Source parameters of small earthquakes recorded at 2.5 km depth, Cajon Pass, southern California: Implications for earthquake scaling, *Geophys. Res. Lett.* **20**, no. 14, 1511–1514.
- Abercrombie, R. E. (1995). Earthquake source scaling relationships from 1 to 5 M_L using seismograms recorded at 2.5 km depth, *J. Geophys. Res.* **100**, no. B12, 24,015–24,036.
- Abercrombie, R. E. (1997). Near-surface attenuation and site effects from comparison of surface and deep borehole recordings, *Bull. Seismol. Soc. Am.* **87**, no. 3, 731–744.
- Abercrombie, R. E. (2015). Investigating uncertainties in empirical Green's function analysis of earthquake source parameters, *J. Geophys. Res.* **120**, no. 6, 4263–4277.
- Abercrombie, R. E. (2021). Resolution and uncertainties in estimates of earthquake stress drop and energy release, *Phil. Trans. Roy. Soc. Lond. A* **379**, no. 2196, 20200131, doi: [10.1098/rsta.2020.0131](https://doi.org/10.1098/rsta.2020.0131).
- Abercrombie, R. E., A. Baltay, S. Chu, T. Taira, D. Bindu, O. Boyd, X. Chen, E. Cochran, E. Devin, D. Dreger, *et al.* (2024). Overview of the SCEC/USGS community stress drop validation study using the 2019 Ridgecrest earthquake sequence, *Bull. Seismol. Soc. Am.* (in revision).
- Abercrombie, R. E., S. Bannister, J. Ristau, and D. Doser (2016). Variability of earthquake stress drop in a subduction setting, the Hikurangi Margin, New Zealand, *Geophys. J. Int.* **208**, 306–320.
- Abercrombie, R. E., D. T. Trugman, P. M. Shearer, X. Chen, J. Zhang, C. N. Pennington, J. L. Hardebeck, T. H. Goebel, and C. J. Ruhl (2021). Does earthquake stress drop increase with depth in the crust? *J. Geophys. Res.* **126**, no. 10, e2021JB022314, doi: [10.1029/2021JB022314](https://doi.org/10.1029/2021JB022314).
- Allmann, B. P., and P. M. Shearer (2009). Global variations of stress drop for moderate to large earthquakes, *J. Geophys. Res.* **114**, no. B1, doi: [10.1029/2008JB005821](https://doi.org/10.1029/2008JB005821).
- Anderson, J. G. (1986). Implication of attenuation for studies of the earthquake source, in *Earthquake Source Mechanics*, S. Das, J. Boatwright, and C. H. Scholz (Editors), Vol. 37, American Geophysical Union (AGU), Washington, D.C., 311–318.
- Anderson, J. G., and S. E. Hough (1984). A model for the shape of the Fourier amplitude spectrum of acceleration at high frequencies, *Bull. Seismol. Soc. Am.* **74**, no. 5, 1969–1993.
- Andrews, D. (1986). Objective determination of source parameters and similarity of earthquakes of different size, in *Earthquake Source Mechanics*, S. Das, J. Boatwright, and C. H. Scholz (Editors), Vol. 37, American Geophysical Union (AGU), Washington, D.C., 259–267.
- Atkinson, G. M., and I. Beresnev (1997). Don't call it stress drop, *Seismol. Res. Lett.* **68**, no. 1, 3–4.
- Baltay, A., R. Abercrombie, S. Chu, and T. Taira (2024). The SCEC/USGS community stress drop validation study using the 2019 Ridgecrest earthquake sequence, *Seismica* **3**, no. 1, doi: [10.26443/seismica.v3i1.1009](https://doi.org/10.26443/seismica.v3i1.1009).
- Benz, H. M., A. Frankel, and D. M. Boore (1997). Regional Lg attenuation for the continental United States, *Bull. Seismol. Soc. Am.* **87**, no. 3, 606–619.
- Bethmann, F., N. Deichmann, and P. M. Mai (2012). Seismic wave attenuation from borehole and surface records in the top 2.5 km beneath the city of Basel, Switzerland, *Geophys. J. Int.* **190**, no. 2, 1257–1270.
- Beyreuther, M., R. Barsch, L. Krischer, T. Megies, Y. Behr, and J. Wassermann (2010). ObsPy: A Python toolbox for seismology, *Seismol. Res. Lett.* **81**, no. 3, 530–533.
- Bindi, D., K. Mayeda, D. Spallarossa, M. Picozzi, A. Oth, P. Morasca, and W. R. Walter (2024). Numerical tests to evaluate the effect of constraining the spectral shape of reference events on source parameter scaling, *Bull. Seismol. Soc. Am.* doi: [10.1785/0120240132](https://doi.org/10.1785/0120240132).

- Bindi, D., D. Spallarossa, M. Picozzi, and P. Morasca (2020). Reliability of source parameters for small events in central Italy: Insights from spectral decomposition analysis applied to both synthetic and real data, *Bull. Seismol. Soc. Am.* **110**, no. 6, 3139–3157.
- Bindi, D., D. Spallarossa, M. Picozzi, A. Oth, P. Morasca, and K. Mayeda (2023). The community stress-drop validation study-part II: Uncertainties of the source parameters and stress drop analysis, *Seismol. Soc. Am.* **94**, no. 4, 1992–2002.
- Boatwright, J. (1978). Detailed spectral analysis of two small New York state earthquakes, *Bull. Seismol. Soc. Am.* **68**, no. 4, 1117–1131.
- Boatwright, J. (1980). A spectral theory for circular seismic sources; simple estimates of source dimension, dynamic stress drop, and radiated seismic energy, *Bull. Seismol. Soc. Am.* **70**, no. 1, 1–27.
- Boore, D. (1986). The effect of finite bandwidth on seismic scaling relationships, in *Earthquake Source Mechanics*, S. Das, J. Boatwright, and C. H. Scholz (Editors), Vol. 37, American Geophysical Union (AGU), Washington, D.C., 275–283.
- Boore, D. M., and W. B. Joyner (1997). Site amplifications for generic rock sites, *Bull. Seismol. Soc. Am.* **87**, no. 2, 327–341.
- Brune, J. N. (1970). Tectonic stress and the spectra of seismic shear waves from earthquakes, *J. Geophys. Res.* **75**, no. 26, 4997–5009.
- Campbell, K. W., and Y. Bozorgnia (2014). NGA-West2 ground motion model for the average horizontal components of PGA, PGV, and 5% damped linear acceleration response spectra, *Earthq. Spectra* **30**, no. 3, 1087–1115.
- Castro, R., J. Anderson, and S. Singh (1990). Site response, attenuation and source spectra of S waves along the Guerrero, Mexico, subduction zone, *Bull. Seismol. Soc. Am.* **80**, no. 6A, 1481–1503.
- Catchings, R. (1999). Regional V_p , V_s , V_p/V_s , and Poisson's ratios across earthquake source zones from Memphis, Tennessee, to St. Louis, Missouri, *Bull. Seismol. Soc. Am.* **89**, no. 6, 1591–1605.
- Chang, H., R. E. Abercrombie, N. Nakata, C. N. Pennington, K. B. Kemna, E. S. Cochran, and R. M. Harrington (2023). Quantifying site effects and their influence on earthquake source parameter estimations using a dense array in Oklahoma, *J. Geophys. Res.* **128**, e2023JB027144, doi: [10.1029/2023JB027144](https://doi.org/10.1029/2023JB027144).
- Chang, H., Q. H. Z. Zhang, N. Nakata, and R. Abercrombie (2025). Investigation of site amplifications using ambient-noise-derived shallow velocity structures under a dense array in Oklahoma, (under review).
- Clouser, R. H., and C. A. Langston (1991). Q_p - Q_s relations in a sedimentary basin using converted phases, *Bull. Seismol. Soc. Am.* **81**, no. 3, 733–750.
- Cocco, M., E. Tinti, and A. Cirella (2016). On the scale dependence of earthquake stress drop, *J. Seismol.* **20**, 1151–1170.
- Cochran, E. S., A. Wickham-Piotrowski, K. B. Kemna, R. M. Harrington, S. L. Dougherty, and A. F. Peña Castro (2020). Minimal clustering of injection-induced earthquakes observed with a large-n seismic array, *Bull. Seismol. Soc. Am.* **110**, no. 5, 2005–2017.
- Crain, K. D., and J. C. Chang (2018). Elevation map of the top of the crystalline basement in Oklahoma and surrounding states. *Oklahoma Geol. Surv. Open-File Rept. OF1-2018*.
- Dougherty, S. L., E. S. Cochran, and R. M. Harrington (2019). The Large-N seismic survey in Oklahoma (LASSO) experiment, *Seismol. Res. Lett.* **90**, no. 5, 2051–2057.
- Edwards, B., and A. Rietbrock (2009). A comparative study on attenuation and source-scaling relations in the Kantō, Tokai, and Chubu regions of Japan, using data from Hi-Net and KiK-Net, *Bull. Seismol. Soc. Am.* **99**, no. 4, 2435–2460.
- Eshelby, J. D. (1957). The determination of the elastic field of an ellipsoidal inclusion, and related problems, *Proc. Math. Phys. Sci.* **241**, no. 1226, 376–396.
- Hanks, T. C., and H. Kanamori (1979). A moment magnitude scale, *J. Geophys. Res.* **84**, no. B5, 2348–2350.
- Hartzell, S. H. (1978). Earthquake aftershocks as Green's functions, *Geophys. Res. Lett.* **5**, no. 1, 1–4.
- Hartzell, S. H. (1992). Site response estimation from earthquake data, *Bull. Seismol. Soc. Am.* **82**, no. 6, 2308–2327.
- Hauksson, E., and P. M. Shearer (2006). Attenuation models (Q_p and Q_s) in three dimensions of the southern California crust: Inferred fluid saturation at seismogenic depths, *J. Geophys. Res.* **111**, no. B5, doi: [10.1029/2005JB003947](https://doi.org/10.1029/2005JB003947).
- Heran, W. D., G. N. Green, and D. B. Stoeser (2003). A digital geologic map database for the state of Oklahoma, *U.S. Geol. Surv. Open-File Rept. 2003-247*, Denver, Colorado, doi: [10.3133/ofr03247](https://doi.org/10.3133/ofr03247).
- Hough, S. (1997). Empirical Green's function analysis: Taking the next step, *J. Geophys. Res.* **102**, no. B3, 5369–5384.
- Hough, S., and J. Anderson (1988). High-frequency spectra observed at Anza, California: implications for Q structure, *Bull. Seismol. Soc. Am.* **78**, no. 2, 692–707.
- Huang, Y., W. L. Ellsworth, and G. C. Beroza (2017). Stress drops of induced and tectonic earthquakes in the central United States are indistinguishable, *Sci. Adv.* **3**, no. 8, e1700772, doi: [10.1126/sciadv.1700772](https://doi.org/10.1126/sciadv.1700772).
- Ji, C., R. J. Archuleta, and Y. Wang (2022). Variability of spectral estimates of stress drop reconciled by radiated energy, *Bull. Seismol. Soc. Am.* **112**, no. 4, 1871–1885.
- Johnson, K. S., and K. V. Luza (2008). *Earth Sciences and Mineral Resources of Oklahoma*, Oklahoma Geological Survey, Norman, Oklahoma.
- Jongmans, D., and P. E. Malin (1995). Microearthquake S-wave observations from 0 to 1 km in the Varian well at Parkfield, California, *Bull. Seismol. Soc. Am.* **85**, no. 6, 1805–1820.
- Kemna, K., A. Peña Castro, R. Harrington, and E. S. Cochran (2020). Using a large-n seismic array to explore the robustness of spectral estimations, *Geophys. Res. Lett.* **47**, no. 21, e2020GL089342, doi: [10.1029/2020GL089342](https://doi.org/10.1029/2020GL089342).
- Kemna, K. B., A. Verdecchia, and R. M. Harrington (2021). Spatio-temporal evolution of earthquake static stress drop values in the 2016–2017 central Italy seismic sequence, *J. Geophys. Res.* **126**, no. 11, e2021JB022566, doi: [10.1029/2021JB022566](https://doi.org/10.1029/2021JB022566).
- Ko, Y.-T., B.-Y. Kuo, and S.-H. Hung (2012). Robust determination of earthquake source parameters and mantle attenuation, *J. Geophys. Res.* **117**, no. B4, doi: [10.1029/2011JB008759](https://doi.org/10.1029/2011JB008759).
- Ktenidou, O., N. Abrahamson, R. Darragh, and W. Silva (2016). A methodology for the estimation of kappa (κ) from large datasets, example application to rock sites in the NGA-East database, and implications on design motions, *PEER Rept. 2016/01*.
- Ktenidou, O.-J., N. A. Abrahamson, S. Drouet, and F. Cotton (2015). Understanding the physics of kappa (κ): Insights from a downhole array, *Geophys. J. Int.* **203**, no. 1, 678–691.

- Levandowski, W., O. S. Boyd, D. AbdelHameid, and D. E. McNamara (2021). Crustal seismic attenuation of the central United States and Intermountain West, *J. Geophys. Res.* **126**, no. 12, e2021JB022097, doi: [10.1029/2021JB022097](https://doi.org/10.1029/2021JB022097).
- Madariaga, R. (1976). Dynamics of an expanding circular fault, *Bull. Seismol. Soc. Am.* **66**, no. 3, 639–666.
- Mayeda, K., L. Malagnini, and W. R. Walter (2007). A new spectral ratio method using narrow band coda envelopes: Evidence for non-self-similarity in the Hector Mine sequence, *Geophys. Res. Lett.* **34**, no. 11, doi: [10.1029/2007GL030041](https://doi.org/10.1029/2007GL030041).
- Newville, M., T. Stensitzki, D. B. Allen, M. Rawlik, A. Ingargiola, and A. Nelson (2016). LMFIT: Non-linear least-square minimization and curve-fitting for Python, *Astrophysics Source Code Library*, record [ascl:1606.014](https://ascl.net/1606.014).
- Nye, T., V. J. Sahakian, E. King, A. Baltay, and A. Klimasewski (2023). Estimates of κ_0 and effects on ground motions in the San Francisco Bay Area, *Bull. Seismol. Soc. Am.* **113**, no. 2, 823–842.
- Oth, A., D. Bindi, S. Parolai, and D. Di Giacomo (2011). Spectral analysis of K-NET and KiK-net data in Japan, Part II: On attenuation characteristics, source spectra, and site response of borehole and surface stations, *Bull. Seismol. Soc. Am.* **101**, no. 2, 667–687.
- Oth, A., H. Miyake, and D. Bindi (2017). On the relation of earthquake stress drop and ground motion variability, *J. Geophys. Res.* **122**, no. 7, 5474–5492.
- Parolai, S., C. G. Lai, I. Dreossi, O.-J. Ktenidou, and A. Yong (2022). A review of near-surface Q_s estimation methods using active and passive sources, *J. Seismol.* **26**, no. 4, 823–862.
- PEER (2015). NGA-East: Median ground-motion models for the Central and Eastern North America Region, *Pacific Earthquake Engineering Research Center (PEER) Rept. No. 2015/04*.
- Pennington, C. N., H. Chang, J. L. Rubinstein, R. E. Abercrombie, N. Nakata, T. Uchide, and E. S. Cochran (2022). Quantifying the sensitivity of microearthquake slip inversions to station distribution using a dense nodal array, *Bull. Seismol. Soc. Am.* **112**, no. 3, 1252–1270.
- Prieto, G. A. (2022). The multitaper spectrum analysis package in Python, *Seismol. Res. Lett.* **93**, no. 3, 1922–1929.
- Rubinstein, J. L., W. L. Ellsworth, and S. L. Dougherty (2018). The 2013–2016 induced earthquakes in Harper and Sumner Counties, southern Kansas, *Bull. Seismol. Soc. Am.* **108**, no. 2, 674–689.
- Shearer, P. M. (2009). Surface waves and normal modes: Rayleigh waves, in *Introduction to Seismology*, Cambridge University Press, Cambridge, United Kingdom, 219–224.
- Shearer, P. M., R. E. Abercrombie, D. T. Trugman, and W. Wang (2019). Comparing EGF methods for estimating corner frequency and stress drop from P wave spectra, *J. Geophys. Res.* **124**, no. 4, 3966–3986.
- Shearer, P. M., G. A. Prieto, and E. Hauksson (2006). Comprehensive analysis of earthquake source spectra in southern California, *J. Geophys. Res.* **111**, no. B6, doi: [10.1029/2005JB003979](https://doi.org/10.1029/2005JB003979).
- Shearer, P. M., I. Vandever, W. Fan, R. E. Abercrombie, D. Bindi, G. Calderoni, X. Chen, W. Ellsworth, R. Harrington, Y. Huang, et al. (2024). Earthquake source spectra estimates vary widely for two Ridgecrest aftershocks because of differences in attenuation corrections, *Bull. Seismol. Soc. Am.* doi: [10.1785/0120240134](https://doi.org/10.1785/0120240134).
- Singh, S., and R. B. Herrmann (1983). Regionalization of crustal coda Q in the continental United States, *J. Geophys. Res.* **88**, no. B1, 527–538.
- Supino, M., G. Festa, and A. Zollo (2019). A probabilistic method for the estimation of earthquake source parameters from spectral inversion: Application to the 2016–2017 central Italy seismic sequence, *Geophys. J. Int.* **218**, no. 2, 988–1007.
- Toksöz, M., D. H. Johnston, and A. Timur (1979). Attenuation of seismic waves in dry and saturated rocks: I. Laboratory measurements, *Geophysics* **44**, no. 4, 681–690.
- Trugman, D. T., S. X. Chu, and V. C. Tsai (2021). Earthquake source complexity controls the frequency dependence of near-source radiation patterns, *Geophys. Res. Lett.* **48**, no. 17, e2021GL095022, doi: [10.1029/2021GL095022](https://doi.org/10.1029/2021GL095022).
- U.S. Geological Survey (USGS) (2022). Earthquake hazards program advanced national seismic system (ANSS) comprehensive catalog of earthquake events and products: Catalog ($M > 3.6$) in central Oklahoma, (2016-04-14–2016-05-10) (data set), available at <https://earthquake.usgs.gov/earthquakes/map/?extent=33.11915,-100.87646&extent=37.09024,-92.0874&range=search&sort=largest&timeZone=utc&search=%7B%22name%22: 2%22Search%20Results%22,%22params%22:%7B%22starttime%22:222016-04-14%2000:00:00%22,%22endtime%22:%222016-05-10%2023:59:59%22,%22maxlatitude%22:36.262,%22minlatitude%22:33.98,%22maxlongitude%22:-94.438,%22minlongitude%22:-98.525,%22minmagnitude%22:3.6,%22orderby%22:%22magnitude%22%7D%67 D> (last accessed September 2022)
- Van Houtte, C., S. Drouet, and F. Cotton (2011). Analysis of the origins of κ (kappa) to compute hard rock to rock adjustment factors for GMPEs, *Bull. Seismol. Soc. Am.* **101**, no. 6, 2926–2941.
- White, M. C., H. Fang, N. Nakata, and Y. Ben-Zion (2020). PyKonal: A Python package for solving the eikonal equation in spherical and Cartesian coordinates using the fast marching method, *Seismol. Res. Lett.* **91**, no. 4, 2378–2389.
- Winkler, K. W., and A. Nur (1982). Seismic attenuation: Effects of pore fluids and frictional-sliding, *Geophysics* **47**, no. 1, 1–15.
- Zalachoris, G., E. M. Rathje, and J. G. Paine (2017). V_{s30} characterization of Texas, Oklahoma, and Kansas using the P-wave seismogram method, *Earthq. Spectra* **33**, no. 3, 943–961.

Manuscript received 21 June 2024

Published online 3 January 2025